Review

An Overview of Snow Water Equivalent: Methods, Challenges, and Future Outlook

Mercedeh Taheri * and Abdolmajid Mohammadian

Department of Civil Engineering, University of Ottawa, Ottawa, ON K1N 6N5, Canada
* Correspondence: mtahe067@uottawa.ca

Abstract: The snow depth or snow water equivalent affects water, carbon, and energy cycles as well as surface–atmosphere interactions. Therefore, the global monitoring of spatiotemporal changes in snow water equivalent is a crucial issue, which is performed by characterizing the macrophysical, microstructural, optical, and thermal characteristics of the snowpack. This paper is a review of the retrieval methods of snow water equivalent in three main categories, including in situ measurements, reconstruction approaches, and space-borne measurements, along with their basic concepts, advantages, and uncertainties. Since satellite observations are the most important tool used to detect snow properties, the paper focuses on inversion models and techniques using microwave remote sensing. The inversion models, based on various theoretical foundations, are classified into empirical, statistical, and physical (emission) models, and the techniques are described in four groups: iterative methods, lookup table, machine learning, and data assimilation approaches. At the end, the available global and regional gridded products providing the spatiotemporal maps of snow water equivalent with different resolutions are presented, as well as approaches for improving the snow data.

Keywords: snow water equivalent; in situ measurements; reconstruction; space-borne measurements; microwave; gridded products

1. Introduction

Snow is a complex medium that experiences considerable changes in space and time, especially in mountainous terrains where both the accumulation process of solid precipitation and the snowpack melting process are highly variable because of the complex topography and diverse land cover types [1]. An accurate estimation of the spatiotemporal changes in snow data is crucial for modeling the global water cycle through the representation of macrophysical, microstructural, optical, and thermal characteristics of the snowpack [2–6]. Snow water equivalent (*SWE*), indicating the amount of water stored in the snowpack, and snow cover area (SCA) are the most critical snow data, which are required for a wide range of purposes, including global water cycle modeling, freshwater management, snow hydrology, meteorology, global change analysis, and risk assessment, such as drought and flood [1,7–15].

SCA information is mostly obtained from the near infrared (NIR) and visible spectral (VIS) wavelengths [16]. The inability of optical signals to penetrate clouds leads to spatiotemporal gaps in SCA retrieval under cloudy weather conditions and high-altitude regions [17]. In addition, SCA is incapable of estimating the snowpack meltwater runoff, which supplies a significant fraction of water resources and determines the dominant hydrological regime in mountain regions [3,10]. *SWE* (or snow depth) monitoring, due to a lack of illumination impact (clouds and nights) [18,19], is more useful than SCA for practical purposes under all-sky conditions. Therefore, the current paper is concerned with the retrieval methods and challenges of *SWE*.

Generally, three approaches have been presented to simulate snowpack variations, including in situ measurements, reconstruction, and space-borne measurements. In situ

SWE measurements include the direct and indirect methods [20]. Direct methods, such as snow pillows, measure *SWE* by weighing the mass of a snow column, while indirect methods of ground-based *SWE* measurement are based on the attenuation of gamma radiation by water molecules. In this way, the difference in gamma radiation levels emitted from the surface (before and after snowfall) is converted to real-time *SWE* via an optimized coefficient. In situ measurement is the most reliable approach for the determination of snow characteristics; however, the limited spatial extent of stations and snow spatial heterogeneities make the method inefficient on a large scale [21,22]. As an alternative method, *SWE* reconstruction is based on a backward melt calculation by the remotely sensed SCA and energy-based snowmelt to temporally and spatially calculate *SWE* for the snow accumulation season [23,24]. Although the in situ data requirement of the reconstruction method is limited, the *SWE* results are only valid for the melt season, leading to its inefficiency for seasonal prediction. Furthermore, the method is sensitive to some factors that can lead to uncertainties if not accurately determined. Those factors include the SCA data, dates of snow disappearance and peak *SWE*, and the snowmelt estimation methods. These factors can lead to uncertainties if they are not accurately determined.

Microwave remote sensing, including active and passive types, is the most significant method to represent spatiotemporal variations of snowpack properties, such as snow depth and snow water equivalent at different scales [17]. Because of the relationship between electromagnetic radiation and snow properties, the snowpack can be simulated with different operating principles and frequencies [25,26]. Compared to active microwave, passive microwave (PMW) remote sensing, which estimates *SWE* based on the brightness temperature (T_B) differences at two different frequencies, has a long-term history due to its global coverage and short revisit time [27–29]. The PMW-based *SWE* measurements date back to 1978 by the Nimbus-7 satellite using the scanning multi-channel microwave radiometer (SMMR) sensor, followed by the inter-calibrated sensors of the special sensor microwave/imager (SSM/I) onboard the Defense Meteorological Satellite Program (DMSP), the advanced microwave scanning radiometer for Earth Observing System (AMSR-E) on the Aqua spacecraft of NASA's Earth Observing System (EOS), AMSR2 on the Japan Aerospace Exploration Agency (JAXA)'s Global Change Observation Mission 1st-Water (GCOM-W1), and the Chinese FengYung series [15].

To understand the relation between PMW brightness temperature and snowpack properties, different inversion models have been developed based on both simple and complicated concepts. Traditional inversion models are defined as the empirical relationships between T_B difference (at two low and high frequencies) and *SWE* [30]. Accordingly, various static and dynamic algorithms have been developed as a result of the different choices of microwave frequency channels as well as coefficient estimation. In the algorithms based on T_B differences, the effect of the physical temperature of snowpack on the brightness temperature is thwarted because of the signal difference, and the saturation effect for thick snow can be also alleviated, to some extent, due to the use of two different low frequencies [31,32]. However, the interlayer scattering intensifies the saturation issue by reason of different electromagnetic characteristics, which leads to temporally inconsistent *SWE* results [31]. An important approach to overcome the weakness of these methods is the use of attenuation concepts of snow radiation, i.e., physically based statistical algorithms and radiative transfer equation (RTE)-based models, and energy and water balance concepts, i.e., land surface models (LSMs) and snowpack modules. The statistical *SWE* retrieval approach is based on a regression relationship between snow water equivalent and snowpack attenuation and radiation properties at different polarizations and frequencies [33]. The RTE-based microwave emission models, as more sophisticated *SWE* estimation structures, are capable of providing snow parameters such as snow depth and density by matching the simulated and observed T_B [34]. These models describing the microwave emission or scattering properties in snow medium and radiative transfer (RT) in the air–snow–soil system are different in many aspects, such as the number of layers, rough or smooth interfaces, grain size parametrization, scattering coefficient, and the solution method of the

RTE [35]. As a general classification, snow emission models have been categorized based on different theoretical foundations including semi-empirical, analytical, and numerical concepts [15]. The semi-empirical approach, which benefits from a simple, stable structure, is based on ground measurements with a limited range of validity. The analytical approach uses Maxwell's equations with physical input parameters; however, it assumes a simplified structure to simulate the snow. In contrast, the numerical approach accounts for certain snow structures, and scattering or emission characteristics are achieved numerically with less simplification. This approach, despite being more time-consuming, provides more accurate simulations in comparison with other types. In addition to snow emission models, the mass and energy balance of the snowpack is used to simulate snow accumulation and melting processes. The most important LSMs are the Biosphere-Atmosphere Transfer Scheme (BATS), Simple Biosphere (SiB), Variable Infiltration Capacity (VIC), Mosaic, and Noah model, which have been discussed in [36]. It should be noted that although LSMs and snowpack simulation modules are capable of estimating *SWE* with some degree of accuracy, the results have shown large uncertainties in space and time [37].

Stand-alone passive microwave *SWE* retrievals have a coarse spatial resolution, and due to this, the spatial variability resulting from mixed land cover and topography cannot be properly captured [38]. This issue is a serious limitation especially in alpine regions with forested cover and deep and wet snowpack so that some PMW products mask out these regions completely [39–42]. To address the matter, the statistical combination of satellite data and in situ observations by data assimilation methods is proposed. The data assimilation approach, which integrates the observations based on their uncertainties, is a promising method to provide *SWE* at continental scales [17,43]. In addition, the nonlinear relationships between PMW brightness temperature and snow parameters can be simulated by several inversion techniques including iterative algorithms, lookup table algorithms, and machine learning algorithms.

On the other hand, the limitation of the coarse spatial resolution of passive microwave can be compensated for by active remote sensing with a higher spatial resolution. Therefore, it is recommended to use active microwave remote sensing rather than passive microwave in alpine regions due to its higher spatial resolution [15]. However, the temporal resolution of active microwave is less than that of passive remote sensing, and it requires the appropriate frequencies (Ku-band) to model the microstructure properties of the snowpack [16]. Two types of inversion algorithms, including physical backscattering and phase-based approaches, are used to estimate snow parameters by using active microwave remote sensing. The physical backscattering composed of surface and volume scattering calculates *SWE* by an iteratively minimized cost function. On the contrary, the phase-based approach uses the repeat-pass SAR measurements to estimate *SWE* through a phase shift caused by snowpack.

This paper is a review of the *SWE* retrieval methods classified into three groups: in situ measurements, the reconstruction method, and space-borne observations, along with their concepts and challenges. In addition, the *SWE* inversion techniques using passive and active microwaves, which are employed to modify the system representation, are described in detail. The available *SWE* products, including satellite-based, data-assimilation-based, and reanalysis data (datasets which that continually updated by the combination of observations and results of prediction models), are also introduced. Eventually, the future outlook of improving *SWE* estimation is discussed. Figure 1 depicts the flow diagram of the current research.

Summarily, the purposes of the manuscript include:

- *SWE* retrieval methods;
- Uncertainty sources;
- Available *SWE* products;
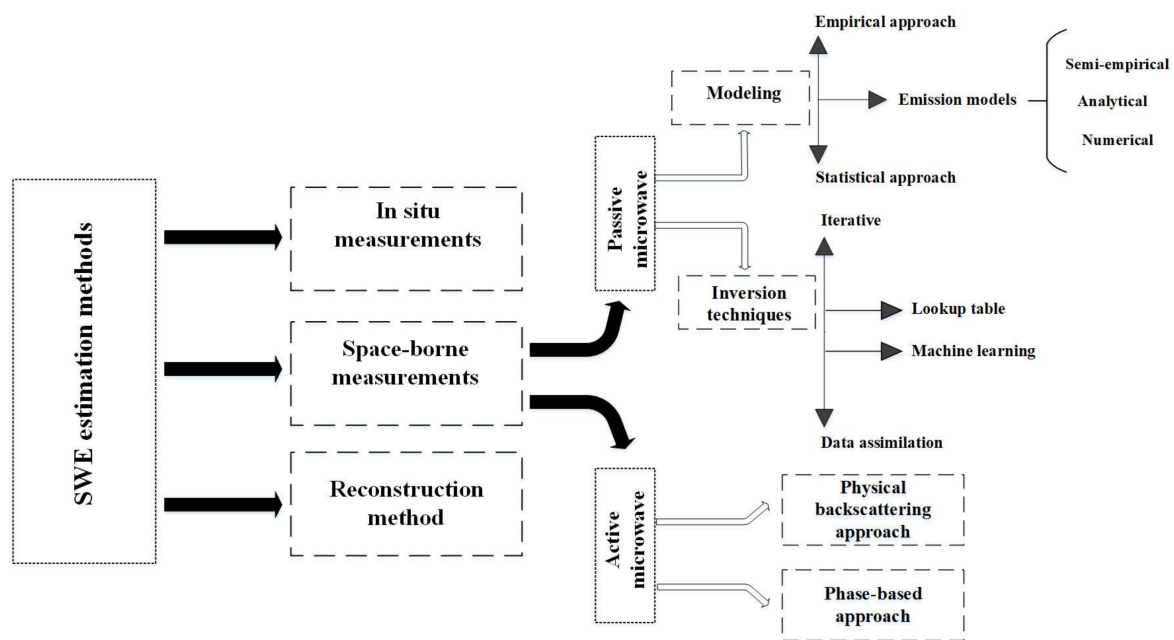- Future outlook and research avenues.

Figure 1. The flow diagram of the current research.

2. In Situ Measurements

The standard method of *SWE* measurement is based on the gravimetric approach, which manually measures the meltwater or weighs the frozen snow sample taken with a snow tube [44]. Snow courses that represent a series of snow sampling points at regular intervals also manually measure *SWE* for each point [13].

Because of the sparse nature of manual measurements, automated methods of *SWE* measurement were proposed to provide continuous amounts. Snow pillows, automated weighing devices [13], are known as the most commonly used method for continuous measuring of *SWE*. Snow pillows are similar to flat circular containers and can last for 10 years or more under normal conditions. Snow water equivalent is continuously achieved by measuring the hydrostatic pressure inside the pillows [45]. Changes in temperature may reduce the accuracy of *SWE* measurements for shallow snow because of the contraction or expansion of the pillow's fluid. This issue, however, is inconsiderable in deep snow, except at the start and end of the snow season [44]. The most reliable measurement by snow pillows is when snow cover is empty of ice layers; otherwise, bridging by frozen snowpack as well as meltwater refreezing can be caused above the pillows [44,46,47]. Therefore, this method is inappropriate during the snowmelt season [47–49].

In addition to snow pillows, radioisotope snow gauges, as a non-destructive approach to sampling, can continuously measure *SWE* and the density profile using a natural radiation source and detector. The method is based on the natural gamma radiation attenuated by snow for a point, a series of points, and a traverse over a region [50]. The difference in gamma radiation levels emitted from the surface is finally converted to *SWE* by an optimized coefficient. Systems with a natural radiation source are usable for both telemetry recording, which is performed by portable gamma-ray spectrometer onboard an aircraft, and in situ measurement, while the gauges using an artificial source for radiation are able to obtain *SWE* only for the site where it is installed. It is important to note that portable gauges measure the snow density by backscatter and present a practical way to dig deep snow pits [51]. This method, which has no radiation risk, unlike the artificial radiation source, is usable for snowpacks with up to 500 mm water equivalent.

The accuracy of point measurements of *SWE* is sensitive to the properties of snowpack, topography variations, and the assumptions or methodologies used (e.g., [39,52–55]).

Some studies showed that snow tubes overestimate *SWE* (e.g., [56,57]) while [58] and [59] found the underestimation of snow tubes in measuring *SWE*. On the other hand,

the snow pillow method has uncertainties ranging from 6% to 12% in measuring *SWE* quantities [60]. Moreover, the natural gamma radiation method has exhibited an average accuracy of ± 20 mm if it is corrected for soil moisture variations in the 10 to 20 cm surface soil layer [44].

The in situ measurement stations, such as snow pillows and courses, are mostly installed near flat terrain sheltered from the wind, which leads to a poor representation of snow accumulation and melting in highlands [61]. With dense enough measurement networks placed in optimized locations, however, interpolation schemes (two or three dimensions) can provide a relatively accurate *SWE* spatial distribution [14]. In this regard, different statistical models, such as kriging, inverse-distance weighting (IDW), multivariate linear regression, etc., have been developed to interpolate point *SWE* measurements. Some studies showed that linear-regression-based methods have better accuracy than simple kriging and IDW [62,63]; however, these methods are incapable of providing a smooth spatial distribution and necessarily establish a linear relationship between the independent variables and *SWE* [64]. Another category consists of the nearest-neighbor-based algorithms, which are well-known due to the nonparametric learning basis and ease of execution [65]. In addition to the low computational effort, the nearest-neighbor-based models can preserve spatiotemporal patterns of *SWE* observations with superior accuracy [64].

A common problem with the interpolation methods is that the snow values may be achieved beyond the actual snowy areas. To attain the physically realistic *SWE* values, interpolation is recommended to be constrained by snow cover area information obtained from remotely sensed images [63]. Nevertheless, some studies showed that bias in point to area interpolation is unavoidable, partly due to the weakness of measured *SWE* in representing the pixels [13]. For example, the authors of [61] showed that 26 assessments among 53 at 15 snow courses and pillows had biases larger than 10%. Molotch and Bales (2005) [66] reported the failure of a snow telemetry site because *SWE* was overestimated by up to 200%. In addition, a significant snow coverage may remain in higher elevations after all snow pillows are bare, showing that stations underestimate some parts of the region [14]. Given that the point measurement for an interpolated product represents the entire grid cell, assessing the topographic effects on melt energy and wind registration can control *SWE* variations of the grid cell at hillslope and watershed scales [1].

3. Reconstruction Method

SWE reconstruction, first introduced by the authors of [67], is a dataset estimated by historical *SWE* information of past snowmelt seasons [24,68]. For this purpose, the snow cover area and energy required for a pure snowpack melt are employed to back-integrate *SWE* from the snowmelt date to the date at which *SWE* reaches its maximum. The reconstruction method is capable of providing spatiotemporal patterns of *SWE* over large and mountainous areas (e.g., [23,24,69–73]). It should be noted that the precipitation is not accounted for during the melt season, causing the bias in the estimates [74].

Basically, the method is based on the snow surface energy balance to calculate snowmelt as follows:

$$M_p \rho L = R_s(1 - \alpha) + R_{l,in} - R_{l,out} + H + LE \tag{1}$$

where M_p is the potential snowmelt (m), ρ is the density (kg/m^3), L is the latent heat of fusion (kJ/kg), R_s is the solar insolation (J/m^2), α is the albedo (dimensionless), $R_{l,in}$ is the incoming longwave radiation (J/m^2), $R_{l,out}$ is the outgoing longwave radiation (J/m^2), H is the sensible heat flux (J/m^2), and LE is the latent heat flux (J/m^2). The short and long wavelengths vary between 0.4 to 1.7 μm and 8 and 14 μm. In addition to full energy balance, the snowmelt rate can be obtained from the temperature index and the combined method of radiation balance and temperature index.

To calculate the actual snowmelt (M_a), M_p is scaled using the snow cover area as follows:

$$M_a = M_p \times SCA \tag{2}$$

where *SCA* is the fractional snow cover area obtained from optical remote sensing. Finally, the *SWE* time series are obtained from back integrating the snowmelt using Equation (3):

$$SWE_0 = SWE_n + \sum_{i=1}^{n} M_{a,i} \tag{3}$$

where SWE_0 is the initial *SWE*, SWE_n is *SWE* at time n, and $M_{a,i}$ is the actual snowmelt during time step i. It should be noted that the SWE_0 for each pixel can be reconstructed at the time when snow is no longer observed (i.e., *SCA* = 0):

$$SWE_0 = \sum_{i=1}^{n} M_{a,i} \text{when } SWE_n = 0 \tag{4}$$

According to the algorithm's structure, by which the snowpack is reversely simulated from the snowmelt period back to peak accumulation, the method can be assessed only after the snow disappearance and is only valid for the melt season. For this reason, the reconstruction method is more appropriate for generating the historical *SWE* reanalysis data (i.e., datasets that are continually updated from past to present) rather than the forecasting of climatological and hydrological variables. Furthermore, the snow disappearance date can be obscured because of cloud cover. This method is suitable only for areas with insignificant snow accumulation during the melt period because the snowmelt depth derived from surface energy balance is valid for the surface layer [75].

Despite the aforementioned disadvantages, the method can be implemented without the need for extensive ground-based observations over whole mountain ranges for decades of time with a high spatial resolution [73]. In addition, the reconstructed *SWE* results can be used as an independent data source to compare with other models.

Sources of Uncertainty in Reconstruction Method

Several factors cause uncertainties in reconstructed *SWE* estimates, including the spatiotemporal resolution of SCA data, the methods used to determine the date of snow disappearance and peak snowfall, and the methods used to calculate the melt rate [14].

Given that the accuracy of the *SWE* reconstruction method increases with improving SCA information, a tradeoff between the spatial and temporal resolution of reconstructed *SWE* is required. For instance, SCA obtained from Landsat has a spatial resolution of 30 m and a time revisit period of 16 days. Although the spatial resolution of SCA is accurate, the presence of cloud cover that is probable during the time revisit period can increase the model error because the clear acquisition of data is prolonged [72]. In contrast, Moderate-Resolution Imaging Spectroradiometer (MODIS) represents the daily SCA information with a 500 m (or 1 km) resolution, which is less accurate than the SCA of Landsat. Therefore, it is recommended to merge the products to improve the low temporal resolution of Landsat and low spatial resolution of MODIS [14,75]. In addition, the misidentification of snow cover presence by satellite products leads to large unrealistic *SWE* values and thereby introduces uncertainty in *SWE* estimation. In this way, accurate determination of the date when snow cover goes to zero is critical. SCA products with a relatively coarse spatial resolution (such as 500 m) are incapable of determining the actual date of snow disappearance due to the gradual decline of the snow fraction. Dozier et al. (2008) [76] suggested that the use of multiproducts, such as MODIS and Landsat, can improve the snowmelt-out date, as the finer temporal resolution reduces the cloud cover effect, which may conceal the actual date.

On the other hand, the maximum SCA does not necessarily represent the peak *SWE*, as the maximum snow depth itself precedes maximum *SWE* owing to the compression of the snowpack over time. The most reliable method for determining the peak *SWE* date is the use of snow pillow data, which leads to an accurate *SWE* product being reconstructed [24]. Although the lack of ground measurements makes the determination of the peak *SWE* date difficult, back-calculating the daily melt provides an upper bound for *SWE* accumulation.

The most considerable uncertainty of the reconstruction approach is related to the data and methods utilized to obtain the melt rate, i.e., the full energy balance, temperature

index, and their combination. The surface micrometeorological data required for accurate estimation of snowmelt are shortwave and longwave radiation, humidity, air temperature, and wind speed. Additionally, the accurate surface albedo, which directly affects the solar radiation, can improve the reliability of reconstruction. It is worth noting that the snow albedo can be derived either by remotely sensed products or snow age-based models, which both introduce uncertainties [24].

4. Space-Borne Measurements

4.1. Passive Microwave

By estimating snow parameters spatially and temporally remote sensing can overcome the issues of point measurements [15]. Visible satellite measurements are mainly used to map snow cover based on the highly visible reflectance of snowy surfaces [77], while satellite-based PMW signals, operating with the naturally emitted microwave energy or light, are employed to monitor the global information of snow depth and *SWE* due to their penetration of the snow [78]. Unlike optical remote sensing, insensitivity of the microwave imagery to atmospheric effects and solar illumination results in detecting changes under all-sky conditions. Likewise, the microwave signals can overcome the misdiagnosis of snow and cloud, which makes the method superior to visible and near-infrared measurements [77].

The microwave radiation emitted from the surface, demonstrated as brightness temperature (T_B), is attenuated by the overlaying snowpack. In other words, the snow medium causes the brightness temperature to be scattered or absorbed, resulting in decreased T_B with increased snowpack [79]. Therefore, *SWE* detection is performed using multi-frequency microwave emissions from snow based on extinction characteristics of frequencies; a lower frequency (long wavelength) has less extinction or less scattering effect than a higher frequency (short wavelength) [30]. On the other hand, the absorption effect at microwave frequencies is related to free water in snowpack (dielectric properties), which increases with the snowpack's moisture [79]. This effect results in the ability to differentiate the wet and dry snowpack; dry snow is snowpack with pure ice grains, and wet snow is assumed to be composed of sticky snowflakes because of the uneven distribution of liquid water-coated grains. Additionally, the polarization information of PMW is utilized to distinguish deep and shallow snowpack due to much penetration into the deep snowpack [80].

4.1.1. Sources of Uncertainty in PMW Method

The uncertainty of PMW-based *SWE* information originates from the sensors and retrieval algorithms. The passive microwave radiometers mostly provide the *SWE* estimates at a very coarse spatial resolution [77], as microwave emissions with low-energy levels require a wide spatial extent to supply enough energy for achieving specified accuracy [14]. This low spatial resolution allows a single grid cell to include different land cover types and heterogeneous snowpacks, making the results inadequate to meet the requirements of a small scale [81,82]. Due to this, *SWE* estimation should be based on the thermal and emissive properties of different land cover types, and the polarization and frequency effects should be considered under different conditions by model-derived or empirical coefficients [83]. However, most algorithms ignore the mixed pixel problem and treat snow as a pure pixel, causing a decrease in *SWE* estimation accuracy. It should be noted that downscaling methods for brightness temperature, such as the mixed pixel decomposition method [84–87] and the enhanced resolution reconstruction method [88,89], can be helpful to reduce the mixed pixel problem, but these methods themselves have uncertainness affecting *SWE* retrieval accuracy.

From the viewing angle of a sensor, the forest areas are composed of the canopy fraction and gap fraction between the canopies. Snow contribution in the microwave observations is based on the gap fraction viewed by the passive sensor; the greater the viewing angle, the more minor the gap fraction [90]. Therefore, the increased canopy fraction, which

results from decreasing the gap fraction in the scene, causes an underestimation of *SWE* because the snow brightness temperature gradient between frequencies decreases. To prove this issue, Vuyovich et al. (2014) [91] showed a better correlation between simulated and PMW-based *SWE* when the canopy fraction is small. In addition to forests, the lake area fraction has a considerable influence on *SWE* retrievals using the T_B difference [32,92]. According to Lemmetyinen et al. (2011) [93], *SWE* estimation accuracy improved when the lake area was considered, likely due to different emissive behaviors of water and snow.

In addition to systematical biases of satellites, the retrieval algorithms are incapable of simulating very thin snowpack (less than a few centimeters) due to the significantly small spectral gradient that occurs between two frequencies. PMW methods also underestimate *SWE* for deep snowpacks [94]. With increasing *SWE*, T_B of homogeneous snow typically decreases until it becomes saturated when a sufficient thickness of snow is reached. In such a situation, microwave signals cannot penetrate the snowpack [39]. Moreover, microwave radiometry is unable to differentiate the deep snow from shallow, dense snow in some cases. For example, the presence of plate-like depth hoar crystals and ice-crust layers can yield increased microwave scattering and, thereby, an artificially overestimated *SWE* value.

The differences in snow characteristics, such as texture, grain size, and snow stratigraphy, have a significant effect on the estimation accuracy of PMW-based *SWE*. The microwave retrieval usually overestimates the *SWE* of snowpacks with a coarse texture and large grain size because of the increased scattering component of extinction [95]. Similar to large effective grain size, the internal reflections lead to increasing the volume scattering and, thereby, increased *SWE* estimates [40,96]. In addition, the liquid water content in snow, which simply perturbs the signals, conducts the behavior of snow towards wet soil in terms of the signal reflection; consequently, the microwave emission increases, especially during the melt season [97]. For wet snowpack, the brightness temperature obtained from PMW illustrates the emission from near the wet snow surface instead of the ground [98].

On the other hand, the emissive properties of the background beneath the snow can also affect the brightness temperature [82]. Dielectric constant and surface roughness are the most important soil parameters that can cause errors in *SWE* retrieval. Vegetation cover has a masking effect on the signal emitted from the underlying snow cover by contributing to emission, absorption, and scatter [99]. That is why *SWE* in forested regions is underestimated up to 50% (e.g., [39,100]). It should be noted that this issue is intensified for global *SWE* retrieval because most terrains covered with snow are also forested. Therefore, it is required to adjust *SWE* retrieved in forest regions by a forest factor derived from satellite vegetation measurements or databases. For other cover types, likewise, it is necessary to utilize an emission model to assess their effect on *SWE* accuracy. In addition to the aforementioned sources, the existence of particulates, dust, ash, black carbon, and haze in the atmosphere can affect the accuracy of *SWE* retrieved by PMW.

4.1.2. Snow Microwave Scattering and Inversion Models

To conceptualize the PMW brightness temperature and model the *SWE* microwave scattering, various microwave models have been developed based on the T_B differences at two frequencies, showing the radiation scattering changes of snowpack at different wavelengths [101]. The models range from simple, i.e., static and dynamic algorithms with empirical structure, to more sophisticated, i.e., physically based statistical algorithms and emission models, which are explained in the following sub-sections.

Empirical Models

The empirical models include static and dynamic algorithms, which are basically established via the brightness temperature differences at different frequencies. The static algorithms calculate *SWE* (or snow depth) using a linear regression between snow water

equivalent and brightness temperature gradient for a snowpack with temporally and spatially constant properties, as follows:

$$SWE = A + B \times \Delta T_B \tag{5}$$

where *SWE* is the snow water equivalent (mm), ΔT_B is the vertically (or horizontally) polarized brightness temperature difference between low (18 or 19 GHz) and high (37 or 85 GHz) frequency, and *A* and *B* are the offset (mm) and slope (mm/K), respectively. The coefficients *A* and *B* are obtained by fitting with experimental data.

The NASA algorithm [30,102] is the simplest example of an *SWE* static algorithm, which is derived for the SMMR sensor as:

$$SWE = 4.8 \times (T_{B,18H} - T_{B,37H}) \tag{6}$$

where $T_{B,18H}$ and $T_{B,37H}$ indicate the horizontally polarized brightness temperatures (K) at 18 and 37 GHz, respectively. T_B is calculated using RTE for a homogeneous snowpack with a constant snow grain size of 0.3 mm and a constant density of 300 kg/m^3. The NASA algorithm can be used only for *SWE* less than 300 mm because the brightness temperature difference for greater *SWE* becomes saturated. In addition, the model is not suitable for various snow grain sizes except 0.3 mm.

SWE estimation is greatly complicated when the surface is covered with vegetation, as the canopy coverage affects the microwave emitted from the snowpack. To consider the forest effect, the NASA 96 algorithm, which is the extended version of the NASA model, was developed to provide global *SWE* inversion [81]. The algorithm is expressed as follows:

$$SWE = \frac{4.8 \times (T_{B,18H} - T_{B,37H})}{1 - f_c} \tag{7}$$

where f_c is the canopy fraction. The NASA 96 model resulted in a decrease in the *SWE* error from 50% to 15% for North America and a significant increase in the *SWE* retrieval accuracy for Europe [81]. However, both NASA and NASA 96 algorithms are incapable of adequately simulating the snow grain size, which is the most critical parameter to determine the snow volume scattering. Therefore, Foster et al. (2005) [39] developed a new *SWE* model by using two adjusted parameters for considering the effects of grain size and canopy fraction:

$$SWE = F_t \times C_t (T_{B,18H} - T_{B,37H}) \tag{8}$$

where F_t and C_t are the adjustment coefficients for canopy fraction and snow grain size, respectively. Although the algorithm has simulated the snow melting and accumulation process well, considerable errors have been still observed in alpine snow.

The different types of land cover backgrounds have a significant effect on changes in brightness temperature and snow characteristics. For example, Hallikainen (1984) [103] found coefficient B to be equal to 2.9 and 5.4 mm/K for swamps and forests, respectively. The Canada algorithm was developed to accurately estimate *SWE* for regions with complex land terrains. However, the model reported a ±20 mm error for most of the simulated *SWE* compared to the ground-based measurements. In addition, the results showed an underestimation for retrieved *SWE* in the tundra region of Canada and boreal forests with deep snow. The mathematical relationship of the model is defined as follows [94]:

$$SWE = \sum_{j=1}^{n} F_j (A + B \cdot \Delta T_B)_j \tag{9}$$

where F_j indicates the percentage of grassland, deciduous forest, coniferous forest, and sparse forest included in the SSM/I grid cell. The *A* and *B* values are separately fitted for each land type, and the total *SWE* is calculated as the weighted sum of *SWE*s of each land cover type.

In addition to the aforementioned models, several snow depth estimation algorithms, which are appropriate for shallow snowpack, have been developed in China during the past two decades. For example, Cao et al. (1993) [104] adjusted the empirical coefficients of the NASA algorithm using the land cover classification. In addition, the NASA model was modified by considering the effects of precipitation, wet snow, vegetation, frozen ground, and cold desert [105]. The RMSE values of the modified model were equal to 6.22 and 5.22 cm when SMMR and SSM/I brightness temperatures were used, respectively.

Some researchers reported that including the snow cover fraction data in the depth estimation algorithms led to an improvement in the accuracy of *SWE* retrievals [106,107]. However, these models are incapable of providing the real-time snow depth, as they employ the 8 day snow cover to derive *SWE*. In this regard, a sequence of semi-empirical snow depth algorithms was proposed to estimate real-time *SWE* for mixed pixels [108]. The snow depth estimation method for the mixed pixels is based on the snow depth of pure parts obtained from separate regression for each land cover type:

$$SD = f_{grass} \times SD_{grass} + f_{barren} \times SD_{barren} + f_{forest} \times SD_{forest} + f_{farmland} \times SD_{farmland} \tag{10}$$

where *SD* is the snow depth and *f* is the fraction of land cover. The *SD* parameter is obtained from integrating the snow fraction into the snow depth regression. The results showed an RMSE of 5.6 cm and a bias of ± 5 cm for snow depth retrievals in comparison with station measurements.

Static models can provide relatively accurate and stable snow depth estimates at local scales. However, the lack of data required for regression limits their use at regional or global scales as the models are calibrated only for specific areas. In addition, the models consider the physical properties of snow, such as grain size, depth, and density, to be constant over time and space, while these parameters change as the snow season progresses. Therefore, the dynamic models, in which the effect of internal metamorphism on *SWE* retrieval is considered through defining the dynamic slope B, have been formed to simulate the spatial and temporal changes of the snowpack.

The temperature gradient index (*TGI*) dynamic algorithm proposed by the authors of [109] considers the spatiotemporal variations of snow internal properties with a focus on grain size. Changes in snow grain size are due to constructive metamorphism, especially temperature gradient. In other words, the underlying soil temperature is higher than the snow surface temperature due to the thermal isolation of snow, resulting in a considerable temperature gradient in the snowpack. Following the temperature gradient, a vapor pressure gradient is established that forces water vapor to move upward. The cold surface layers of snow lead to water vapor condensation, and thereby the snow grain size increases. According to Equation (11), *TGI* is a cumulative index from the beginning of the snowfall, showing the grain size growth:

$$TGI = \frac{1}{C} \int_0^t \frac{T_g - T_a}{SD(t)} \mathrm{d}t \tag{11}$$

where *C* is an empirical coefficient (20 °C/m), T_g is the temperature of the soil–snow interface (°C), T_a is the temperature of the atmosphere–snow interface (°C), and $SD(t)$ is the snow depth varying with time (*t*). In addition, Josberger and Mognard (2002) [109] presented a linear relationship between *TGI* and brightness temperature gradient as follows:

$$TG = (T_{B,19H}) - T_{B,37H} = \alpha TGI + \beta \tag{12}$$

where *TG* is the temperature gradient. Finally, the snow depth at time *t* is obtained from Equations (11) and (12):

$$SD(t) = \frac{\alpha(T_g - T_a)}{C\left(\frac{\mathrm{d}TG}{\mathrm{d}t}\right)} \tag{13}$$

The use of the *TGI* model, despite its ability to represent the physical processes during snow evolution and improve the estimation accuracy of snow depth [109,110], is restricted by several issues explained as follows. The model is valid only for conditions where T_g is higher than T_a, and it cannot be applied to areas outside of the original study area due to the lack of in situ data required for model calibration. The differential equation used in the *TGI* algorithm causes errors when daily *SWE* retrieval is targeted; thus, the time series of brightness temperature and air temperature should be smoothed. In addition, the actual snow depth is not simulated correctly when the melting process begins, and a small change in $\frac{dTG}{dt}$ can yield an unreasonably large snow depth.

In addition to the *TGI* model, a dynamic algorithm with a semi-empirical structure was developed by Kelly et al. (2003) [82] to describe the temporal variations of snow volume and grain size using Equations (14) and (15), respectively:

$$f_v(t) = f_{v,\infty} - (f_{v,\infty} - f_{v,0})exp(-lt) \tag{14}$$

$$r(t) = r_\infty - (r_\infty - r_0)exp(-kt) \tag{15}$$

where *r(t)* is the snow grain size (mm), r_0 is the initial snow grain size (mm), r_∞ is the upper limit for snow grain size, *t* is the time (day), *k* and *l* are the empirical coefficient (day^{-1}), f_v *(t)* is the snow volume fraction (%), $f_{v,0}$ is the fresh snow volume fraction (%), and $f_{v,\infty}$ is the maximum f_v (%).

By combining the Dense Medium Radiative Transfer (DMRT) model with snow grain size and density, a quadratic polynomial regression equation was achieved based on the brightness temperature difference and snow depth:

$$SD = b(\Delta T_B)^2 + c\Delta T_B \tag{16}$$

where *SD* is the snow depth (cm), ΔT_B is the vertically polarized brightness temperature difference between 19 and 37 GHz, and *b* and *c* are the empirical coefficients of grain size and snow volume, respectively, which are obtained as follows:

$$b = 0.898\left(\frac{grain\ size}{f_v}\right)^{-3.716} \tag{17}$$

$$c = 1.060\left(\frac{grain\ size}{f_v}\right)^{-1.915} \tag{18}$$

Although the mean error of snow depths simulated by this model is close to zero compared to ground truth data, its RMSE is larger than the static NASA algorithm, and its performance is also more unstable than the NASA 96 model.

Grippa et al. (2004) [110] developed a spatially varying static model by combining the NASA static algorithm and the *TGI* dynamic model. The coefficient *B* in the NASA algorithm was adjusted to match the snow depth obtained from the *TGI* model for each pixel, as follows:

$$B = \frac{SD(t)}{T_{B,19H} - T_{B,37H}} \tag{19}$$

In order to validate the snow depth results, the monthly meteorological data were compared to the simulated monthly snow depth results, showing a reasonable performance [110]. Furthermore, it was found that the algorithm can yield better results when applied to a long-term climate change scale (e.g., monthly) [111].

Given that most of the aforementioned models are appropriate only for shallow snowpack, Kelly (2009) [54] developed a dynamic algorithm to simulate both deep and shallow snowpack by using different frequencies. According to this model, the depth of shallow snowpack is estimated via 19 and 37 GHz, and the deep snow depth is obtained from 19 and 10 GHz. Daily brightness temperature measurements are employed to derive

the scaling factor between ΔT_B and *SWE*. Finally, *SD* is obtained from summing the forested and non-forested components weighted by the forest fraction:

$$\text{SD} = f_f\left(SD_f\right) + \left(1 - f_f\right)\left(SD_0\right) \tag{20}$$

where subscript *f* and *0* indicate forest and non-forest, respectively, f_f is the forest fraction, and *SD* is the snow depth.

Physically Based Statistical Algorithms

    SWE can be derived by a regression relationship with the attenuation properties and snowpack radiation. Multiple scattering in the RTE was firstly considered by Jiang et al. (2007) [112] through the matrix doubling (MD) approach. In the model, the DMRT with Mie scattering is employed to calculate emission and extinction, and the advanced integral equation model (AIEM) is utilized to describe the boundary conditions. The MD model with multiple scattering leads to a numerical solution to RTEs, which is a complex form used to retrieve *SWE*. Therefore, a parameterized model was developed by comparing multiple scattering in the previous model and the form of the zeroth-order model [112]. Since this model is adequate only for snowpack with an optical thickness of less than two, Jiang et al. (2011) [33] proposed a revised version of the model in which a statistical *SWE* retrieval algorithm is used. To eliminate the disturbance from the satellite signals, the model uses the relationships between surface emissivities at different polarizations and frequencies to retrieve *SWE*. In this way, a database composed of snow signals with a large number of combinations of snow parameters is established. Finally, *SWE* is calculated through the regression relationship with the attenuation properties and snowpack radiation obtained from the database:

$$SWE \approx \exp\left(a + b \cdot A' + c \cdot A'^2 + d \cdot \log\left(-\log\left(B'\right)\right)\right) \tag{21}$$

where A' and B' indicate snowpack radiation and attenuation properties, respectively, achieved via dual-polarization brightness temperature at two frequencies. *a*, *b*, *c*, and *d* are coefficients fitted by the database. The comparison of *SWE* results obtained from the physically based statistical algorithm and the operational AMSR-E algorithm showed the overestimation of both models; however, the estimation accuracy of the statistical algorithm was slightly higher than that of the AMSR-E model [33]. It should be noted that the use of newly developed physically based statistical models is limited by dense vegetation, resulting in a need for further modification.

Emission Models

    The emission models are capable of simulating the microwave interactions of the snow–air–soil system, including (i) surface scattering from the snow–ground interface, (ii) volume scattering from snow particles, (iii) the interaction between snow and ground, and (iv) the snow–air interface, both in one layer [112–114] and multi-layers [31,35,96]. In addition, they can treat snow as a continuous medium [96,115–117], clusters of ice spheres [114], or discrete ice spheres [118]. The volume scattering coefficient is also obtained from three types of methods, including the empirical approach [96,113], Monte Carlo simulation [116,119], and analytical approach [114,115,118]. Strong fluctuation theory (SFT) and DMRT theory, which are well-known analytical methods, calculate the scattering coefficients of snow for the continuous medium [115] and ice particles [114,118], respectively. In addition, the bicontinuous model, which is appropriate for the continuous medium of ice and air, employs Monte Carlo simulation to derive the scattering coefficient [116,117]. In order to solve the RTE, the radiation in the 4π space can be separated into two fluxes [120], six fluxes [96], and multiple fluxes using Gaussian quadrature and Eigen analysis [35,114,115]. Generally, emission models have been composed of three major parts under the radiative transfer concept to simulate the snow medium [101]:

- Snow microstructure parameterization

Measuring snow microstructure parameters, which mostly consist of maximum geometrical extent (Dmax) or snow grain size, the correlation length (Pc), and stickiness and optical diameter (D0), is challenging [121]. These parameters affect the determination of electromagnetic properties, such as dielectric constant, absorption, and scattering coefficient. Some structures such as the Microwave Emission Model of Multi-Layer Snow (MEMLS) and the bicontinuous model treat snow as a continuous medium while the models of the Helsinki University of Technology (HUT) and DMRT with Quasicrystalline approximation (QCA) use a set of discrete ice spheres to parameterize the snow microstructure.

- Solution of RTE

Microwave scattering and snow emission are modeled by RTE, which is a partial differential or integral equation. Depending on the number of discrete directions of fluxes, the techniques of RTE solution are classified into three groups: two-stream (such as HUT model), six-stream (such as MEMLS model), and any number of streams defined by the user (such as DMRT model).

- Snow propagation, emission, or scattering estimation

The scattering effect on the brightness temperature and backscattering coefficient is more dominant than absorption. Three types of models, including semi-empirical models, analytical models, and numerical models, have been developed to estimate the emission and scattering effects. The models consider the multiple microwave interactions within the snow and refraction, transmission, and reflection at the interfaces by the RTE on a plane-parallel medium [122,123]. Different types of microwave emission approaches along with the most important models are discussed below:

- Semi-empirical approach

The semi-empirical approach relies on field measurements and calculates the scattering coefficient as a function of incident frequency and snow grain size. The outstanding properties of this approach are its wide and strong practicability, simple structure, and low electromagnetic computations. In the approach, the change of brightness temperature in the propagation directions of θ, φ, and z is achieved using radiative transfer theory, described by the following general expression [29]:

$$\frac{\partial T_B(z,\ \theta,\varphi)}{\partial z \cdot sec\theta} = -\Bbbk_e \cdot T_B(z,\ \theta,\varphi) + \Bbbk_a T + \frac{1}{4\pi} \iint \Bbbk_s^{bi}(\theta,\varphi,\theta',\varphi') . T_B(z,\ \theta',\varphi') \sin\theta' \mathrm{d}\theta' \mathrm{d}\varphi' \tag{22}$$

where θ is the zenith angle, φ is the azimuth angle, z is the vertical location (snow depth), θ' and φ' are slant angles, T_B is the brightness temperature, $\Bbbk_e$ is the extinction coefficient, $\Bbbk_a$ is the absorption coefficient, T is the physical temperature of snow, and $\Bbbk_s^{bi}(\theta,\varphi,\theta',\varphi')$ is the bistatic scattering coefficient. On the right side of the equation, the first term shows the attenuation of microwave emission because of scattering and absorption, the second term exhibits the emitted radiation from snow, and the third term is the sum of scattered microwaves in the direction (θ,φ).

The scattering coefficient $\Bbbk_s$ is the average value of the bistatic scattering factor over 4π space, stated as follows:

$$\Bbbk_s = \frac{1}{4\pi} \int_{\theta'=0}^{\pi} \int_{\varphi'=0}^{2\pi} \Bbbk_s^{bi}(\theta,\varphi,\theta',\varphi') . \sin\theta' \mathrm{d}\theta' \mathrm{d}\varphi' \tag{23}$$

With different RTE solutions and assumptions, HUT and MEMLS models, as the most important semi-empirical models, have been formed as follows:

The Microwave Emission Model of Multi-Layer Snow (MEMLS) [96], which is based on the SFT [124], has a multi-layer structure with intermediate complexity for the 5–100 GHz frequency range. Assuming the snow medium is a parallel plane, Equation (23) can be simplified by reducing the propagation directions of T_B into the direction (θ_0, φ_0) and the

direction $(\theta_0 + \pi, \varphi_0 + \pi)$. In addition, the directions are not generally vertical; therefore, this equation can be stated using two fluxes of upward (up) and downward (dn) direction:

$$\frac{\partial T_{up}(z')}{\partial z'} = -\Bbbk_e \cdot T_{up}(z') + \Bbbk_a T + \Bbbk_s^{forward} T_{up}(z') + \Bbbk_s^{backward} T_{dn}(z') \tag{24}$$

$$-\frac{\partial T_{dn}(z')}{\partial z'} = -\Bbbk_e \cdot T_{dn}(z') + \Bbbk_a T + \Bbbk_s^{forward} T_{dn}(z') + \Bbbk_s^{backward} T_{up}(z') \tag{25}$$

where $z' = z.sec\theta_0$, θ_0 is the observing zenith angle, $T_{up}(z')$ and $T_{dn}(z')$ are the upward and downward brightness temperatures, respectively, and $\Bbbk_s^{forward}$ and $\Bbbk_s^{backward}$ present the forward and backward scattering coefficients, respectively. The sum of $\Bbbk_a$ and $\Bbbk_s$ equals $\Bbbk_e$, and the sum of $\Bbbk_s^{forward}$ and $\Bbbk_s^{backward}$ is $\Bbbk_s$. By using these expressions in the MEMLS model, Equations (24) and (25) are rearranged to:

$$\frac{\partial T_{up}(z')}{\partial z'} = -\Bbbk_a(T_{up}(z') - T) - \Bbbk_s^{backward}(T_{up}(z') - T_{dn}(z')) \tag{26}$$

$$\frac{\partial T_{dn}(z')}{\partial z'} = -\Bbbk_a(T_{dn}(z') - T) - \Bbbk_s^{backward}(T_{dn}(z') - T_{up}(z')) \tag{27}$$

The above RTEs that are employed in the MEMLS model only use the backward scattering coefficient. A six-stream theory is exerted to solve the RTE by considering total coherent, incoherent, and trapped radiation on the snow layer. In other words, the horizontal radiation trapped by internal reflection inside the snowpack is divided into four fluxes, and it includes a total of six fluxes together with upward and downward fluxes [125].

The model simulates snow microstructure via a second-order statistical function by using the exponential correlation length, the derivative of this function. In addition, MEMLS can use both semi-empirical and physically based approaches to determine the volume scattering coefficient. In the semi-empirical approach, the scattering coefficient is achieved by correlation length and snow density, and it can also be computed using the physically based Improved Born Approximation (IBA) method [124]. It should be noted that IBA has been used to model coarse-grained snowpack as a physical extended version of MEMLS. On the other hand, the absorption coefficient is calculated based on two real and imaginary parts which are estimated by an empirical formula and the Polder–van Santen model, respectively.

Another well-known empirical model for simulating snowpack is the Helsinki University of Technology (HUT) model [113], which follows a single-layer structure to simulate snowpack based on the empirical extinction and scattering coefficients fitted with observed grain size. The HUT model is appropriate to simulate the homogeneous, single-layer dry snowpack over large regions using frequencies between 18–90 GHz. The model basically assumes that a forward direction governs the total scattered intensities; therefore, an empirical coefficient q is used to parameterize the scattered incoherent radiation intensity concentrated in the forward direction through the RTE as follows:

$$\frac{\partial T_{up}(z')}{\partial z'} = -\Bbbk_a T + (q\Bbbk_s - \Bbbk_e) T_{up}(z') \tag{28}$$

$$\frac{\partial T_{dn}(z')}{\partial z'} = -\Bbbk_a T + (q\Bbbk_s - \Bbbk_e) T_{dn}(z') \tag{29}$$

Obviously, the HUT model uses a two-flux approximation similar to the MEMLS, i.e., the interfaces between air and snow layers and snow and ground layers reflect both downward and upward emissions; however, the six-stream theory is not included in the HUT model. In HUT, the scattering phase of snow is modeled based on a forward

function, named the Dirac delta function, and the extinction coefficient is obtained from the experiment in the following way [126]:

$$\Bbbk_e = 0.0018 f'^{2.8} d_0^2 \tag{30}$$

where $\Bbbk_e$ is the extinction coefficient (dB), f' is the frequency (GHz), and d_0 is the snow diameter (mm). Roy et al. (2004) [127] improved the extinction function via the Rayleigh scattering expression. It is noteworthy that the brightness temperature values for deep snowpack are underestimated due to the assumption of forward concentration for scattered radiation [101]. On the other hand, the absorption coefficient of snow, similar to the MEMLS, is computed using the dry snow dielectric constant with the real part obtained from Matzler (1987) and the imaginary part obtained from the Polder–van Santen mixture dielectric constant model [98].

Although the model has relatively adequate accuracy in estimating microwave radiation for a single homogeneous layer, averaging the input parameters causes the uncertainty of the results. For that reason, a snow multilayer modification has been applied to the original model to allow the estimation of emission from snow with several layers. The multilayer HUT model [31] can simulate the snowpack with an unlimited number of vertically stacked snow layers by applying the original HUT model to each layer. Furthermore, the modified model makes the estimation of brightness temperature feasible from sea ice or snow-covered lakes. In defining the layered structure, the modified version follows the approach of MEMLS, albeit it omits the coherent components in layer interactions. The interfaces between layers and the topmost snow–air interface are also considered Lambertian.

Generally, the HUT model, due to its strength and simplicity, is known as a widely used structure in passive microwave snow depth inversion algorithms. Despite the MEMLS model, HUT is not recommended for deep snowpacks (>50 cm) because of underestimation of the brightness temperature [101]. Figure 2 depicts the schematic structure of the HUT and MEMLS models for multiple-layer snow.

- Analytical approach

The electromagnetic calculation is a challenging stage of snow microwave emission modeling due to the high density of scatter [122,128,129]. In traditional radiative transfer theory, which is based on the energy conservation law, the snowpack is assumed to be composed of independent scattering spheres. The scattering coefficient of each particle is calculated using Mie theory [130,131], and total scattering magnitude is finally achieved by summing the scattering of all particles. The problem with this method is that it ignores the collective scattering and coherence effect because of the independent simulation of particles. Therefore, the traditional RTE, despite considering the superposition of intensity, is not valid for snow with densely distributed scattering particles [15]. To address this issue, Maxwell's equations, because of their independent approach to snow conditions, are used to derive the appropriate relationships after several approximations, called analytical models [35]. The accuracy and calculation process of analytical models is higher and more complex than that of semi-empirical models, respectively [20].

As the first analytical model, Tsang et al. (1985) [122] developed the Dense Medium Radiative Transfer (DMRT) model to consider the scattering theory of dense mediums by microwave remote sensing. DMRT accounts for the propagating constant, leading to improvement in the extinction coefficient, the propagating constant, single scattering albedo, and scattering phase matrix for dense snow [15]. An overestimation of scattering; however, is caused if the model is used with traditional RT theory. The model can simulate snowpack in both a single-layer (DMRT [122]) and multilayer (DMRT-ML [35]) mediums by treating snow as a collection of spherical ice particles. The schematic structure of the DMRT model for a multi-layer snowpack is presented in Figure 3.
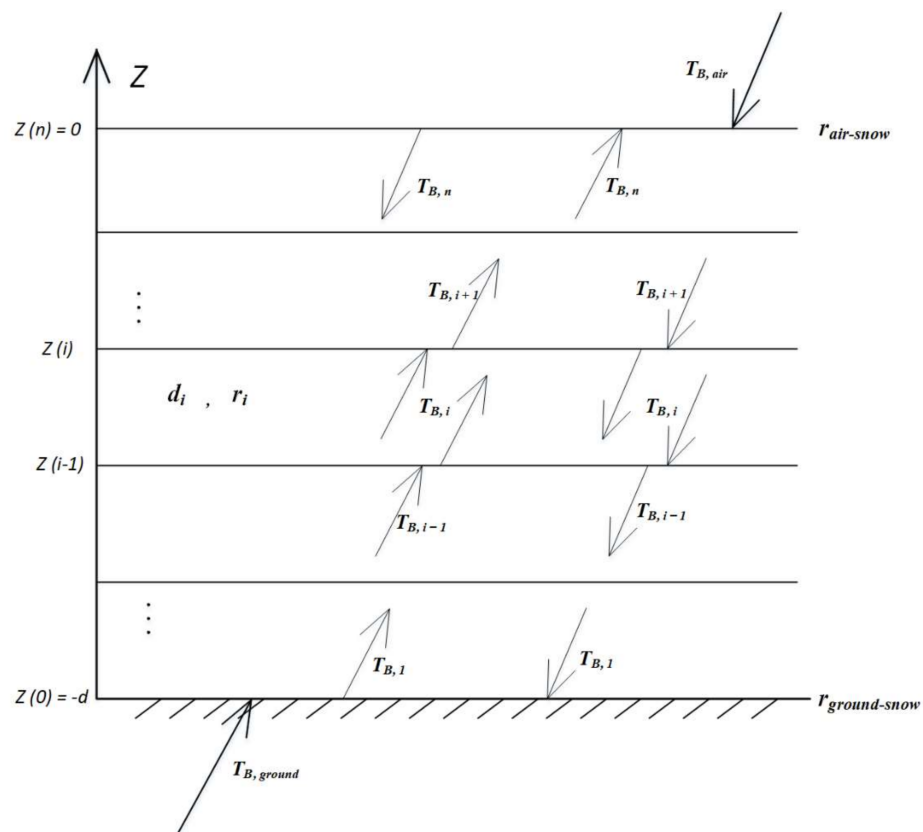
Figure 2. Schematic overview of the HUT and MEMLS models for a snowpack with n layers. In the figure, d_i and r_i are the thickness and reflectivity of layer i, respectively, $T_{B, ground}$ is the upward ground brightness temperature, $T_{B, air}$ is the downward air brightness temperature, $r_{air\text{-}snow}$ is the air–snow boundary reflectivity, and $r_{ground\text{-}snow}$ is the ground–snow boundary reflectivity.

By considering the snowpack as a stack of plane-parallel layers, the RTE for each layer is as follows, as in [132]:

$$\frac{\partial T_B(z,\ \theta,\varphi)}{\partial z \cdot sec\theta} = -\Bbbk_e \times T_B(z,\ \theta,\varphi) + \int_0^{\pi/2} \int_0^{\pi/2} P(\theta,\varphi,\theta',\varphi').\ T_B(z,\ \theta',\varphi') \sin\theta' \mathrm{d}\theta' \mathrm{d}\varphi' + \Bbbk_a T \tag{31}$$

where P is the phase function.

The model calculates the absorption coefficient as a function of density and radius, and estimates scattering and extinction coefficients using the dielectric constant. For dry snow, the dielectric constant is calculated using snow temperature [133,134] while the dielectric constant of the wet snow is achieved by the mixture relationship [135,136]. Unlike the HUT and MEMLS models using the two- and six-stream approach, respectively, most DMRT-based models employ many streams. The discrete-ordinate method can be applied to solve the DMRT equation with a number of streams greater than six.

The laboratory experiments and solutions of Maxwell's equations showed that, in densely packed mediums, the snow particles scatter together because they are dependent on one another [118,137]. In this way, the QCA and Quasicrystalline Approximation with Coherent Potential (QCA-CP), which consider the pair distribution function of the coherent wave interaction and particle positions, are used to account for the correlation between particles. The DMRT-QCA model is mostly employed to simulate moderately sized snow particles through the estimation of the coherent transmission and effective propagation constant [114], while DMRT-QCA-CP is used for snow particle sizes smaller than the wavelength [138]. Accordingly, the model may be inappropriate for large snow grains and frequencies higher than 37 GHz. The simulation of large particles can be implemented by the Mie phase matrix [114]; however, the method is computationally intensive and is

incompatible with the RTE optimization used in DMRT-ML. To overcome the limitation of particle size, accounting for the stickiness between snow spheres instead of randomly non-penetrable spheres leads to coarse-grained snow constitution [35], as well as reducing the needed parameters [139]. The Dense Media Radiative Transfer with Quasicrystalline Approximation (QCA) Mie Scattering of Sticky Spheres (DMRT-QMS) model [117] treats the snowpack as a set of sticky spherical ice particles. It should be noted that the phase function for this case is the same as that for the non-sticky small particles [35]. Moreover, the Dense Media Radiative Transfer with Advanced Integral Equation Model with Matrix Doubling (DMRT-AIEM-MD) model, a multi-frequency radiative model, was developed to simulate the rough interface, in which the propagation of an electromagnetic wave is characterized via DMRT, the scattering from lower and upper surfaces is calculated by AIEM, and the multiple scattering effect is described through the MD method [140]. Although considering a collection of snow particles with different sizes can improve the microstructural representation, the simultaneous formulation of size distribution and stickiness results in a complex quadratic system of equations. In addition to QCA and QCA-CP, the SFT [141], IBA [124], and the effective field approximation (EFA) are other examples of relationships derived from Maxwell's equations. STF and IBA are appropriate for frequencies less than 200 GHz and between 1 and 100 GHz, respectively. EFA, which is a low-order approximation in comparison with QCA and QCA-CP, is suitable for simulating sparse particles as well.
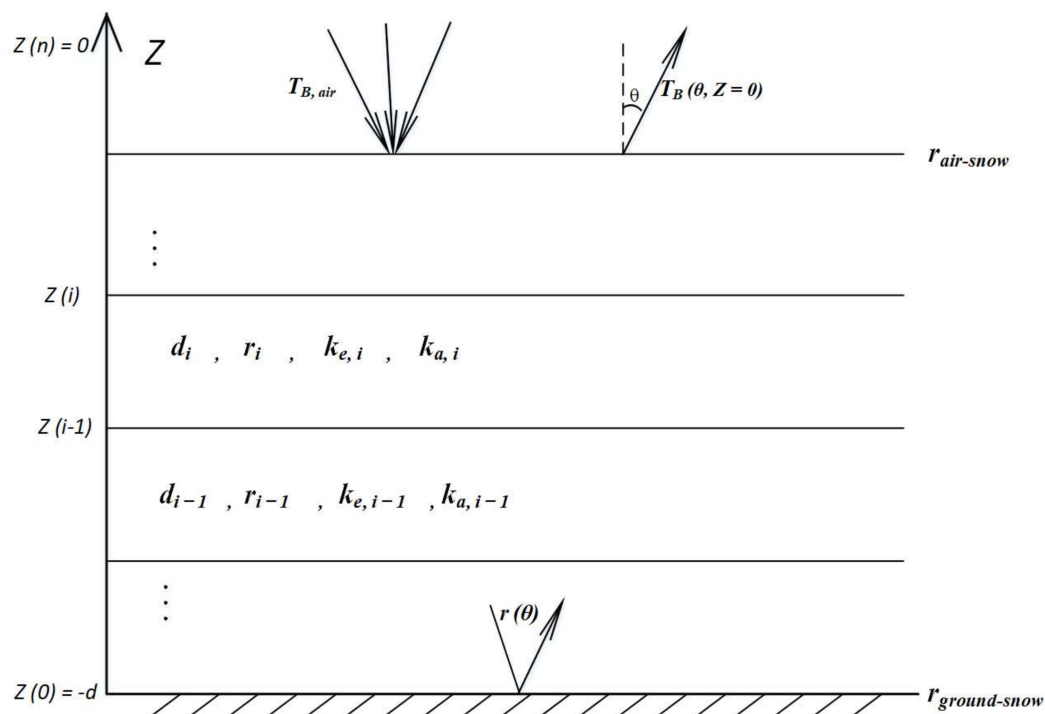
Figure 3. Schematic overview of the DMRT model for a snowpack with n layers. In the figure, d_i and r_i, $k_{e,i}$, and $k_{a,i}$ are the thickness, reflectivity, extinction coefficient, and absorption coefficient of layer i, respectively, $T_{B,air}$ is the downward air brightness temperature, $r_{air-snow}$ is the air–snow boundary reflectivity, $r_{ground-snow}$ is the ground–snow boundary reflectivity, and $T_B(\theta, Z = 0)$ is the brightness temperature of snowpack.

- Numerical approach

    Numerical models, unlike empirical and analytical models, directly calculate the snow scattering properties via numerical electromagnetic computations. These models mostly suffer the disadvantage of requiring time-consuming computational efforts; however, parallel computers can be partly helpful to accelerate the simulation of large-scale numerical

models. The numerical structures eschew the unrealistic assumptions regarding the shape of snow particles, such as the assumption of spherical and regular particles, and this leads to simulations of snow microstructure that are very close to real conditions. In addition, the cross-polarization elements of the phase matrix are considered nonzero because of irregular snow microstructure, resulting in a stronger prediction of the cross-polarization signal, while the analytical models, such as DMRT-QCA underestimate the polarization signal because the cross-polarization elements of the phase matrix are assumed to be equal to zero.

A bicontinuous medium was proposed by Ding et al. (2010) [116] to numerically estimate snow microwave emission and scattering. In this model, the snow structure is treated as the bicontinuous medium, and the Gaussian random field (GRF) and discrete dipole approximation (DDA) are used to simulate the snow microstructure and scattering, respectively. The incoherent field, which is separated from the coherent field by many realizations, is also utilized to calculate the scattering coefficient and phase matrix. Numerical models, such as DMRT bicontinuous, require a time-consuming computational process with few assumptions, and provide results that are close to the actual situations. Furthermore, the numerical structures, similar to analytical models, consider the collective scattering effect and can simulate passive and active microwave radiation and scattering properties.

In addition to snow emission models, the mass-energy balance structures and snow-pack simulation models forced by ground, remotely sensed, and reanalysis data can be exerted to simulate the snow accumulation and melting processes, and thereby the snow depth and *SWE* data. Unlike offline models that lack any interaction between surface and atmosphere, coupled models allow the fluxes to interact between snow surface and atmosphere. Accordingly, the coupled structures provide more accurate simulations than the uncoupled ones, especially in complex topography in which precipitation and radiation are changed with a varied lapse rate [13]. In these models, the precipitation should be separated into rainfall and snowfall, which is mostly performed using the temperature threshold method, to obtain the accumulated snow. In addition, accurate temperature data is critical for determining the snowpack ablation rates. The melt rate also relies on longwave radiation and snow albedo, as the solar radiation component is the most important driver of the melting process. Generally, multilayered snowpack models with greater complexity estimate more precise *SWE*s, as these models better capture the changes in effective factors and driving forces [142].

4.2. SWE *Inversion Techniques Using the Passive Microwave Approach*

The use of the passive microwave approach in retrieving *SWE*, as stated previously, is limited by the effect of forest attenuation, coarse spatial resolution, the saturation effect, and sensitivity to different snow parameters (such as snow density, temperature, grain size, and stratigraphy). These factors make *SWE* retrieval complicated due to the complex nonlinear relationships between brightness temperature and snow depth. Therefore, several inversion techniques, including iterative algorithms, lookup table algorithms, machine learning algorithms, and data assimilation methods, are widely used to improve *SWE* estimation accuracy and presentation of nonlinear relationships between PMW brightness temperature and snow properties. These techniques, which are exhaustively discussed in the following sub-sections, use the emission models and snowpack simulation structures as observational conductors.

Iterative Algorithms

Iterative algorithms have been developed based on a forward model in which *SWE* (or snow depth) is iteratively adjusted to minimize the cost function between the observed and simulated brightness temperature. This approach is capable of simulating the nonlinearity between brightness temperature and *SWE*; thus, its computational effort is extremely high. To reduce the cost, the snow grain size and depth are usually assumed to be variable, and other parameters are considered fixed. The emission models, with the satellite observations of brightness temperature, can estimate snow water equivalent by using an iterative

process. A well-developed model of this approach is the HUT model, which iteratively fits the simulated brightness temperatures with observed values to achieve the cost-minimized *SWE* by the least squares method and constraint condition [113].

Lookup Table Algorithms

A lookup table, which includes inputs and outputs of the snow emission models, can provide snow parameters for estimating *SWE* via seeking the estimated brightness temperature combinations that are similar to T_B observations. The HUT and DMRT-QCA-CP are usually used as the observation models for these algorithms. The efficiency of this search-based approach is based on the searching algorithm employed, which can be a simple searching method without prior knowledge [113,127,143,144] or with prior knowledge [42,145]. Prior knowledge, such as snow grain size, snow depth, snow density, and snow vertical stratigraphy, is utilized to increase the accuracy of the table. For example, Dai et al. (2012) [146] established three lookup tables based on the MEMLS model with prior knowledge. Accordingly, one to three snow layers with brightness temperatures at 10, 18, and 36 GHz frequencies were used to build the lookup tables. In addition, a modified lookup table for forest areas was established by including the snow transmissivity properties related to the forests, which led to an RMSE of 4.5 cm in the northeast forest of China [147]. A substantial feature of this method is its failure potential if a one-to-one correspondence between brightness temperature and *SWE* is not established. It should be noted that this correspondence can be restricted by prior knowledge; however, the absence of knowledge along with the errors of snow emission models limits the application of lookup table algorithms for large regions.

Machine Learning Algorithms

The nonlinear machine learning techniques, such as the artificial neural networks (ANNs), the supported vector machines (SVMs), and random forests (RFs) with prior information, can simulate the complex relationships between PMW brightness temperature and snow parameters. A widely used method to solve the nonlinear relationships is the ANN method, which is a first-order mathematical approximation. ANN models, such as the back propagation (BP) neural network algorithm, can simulate the nonlinear relationship between dual-polarization brightness temperature, multi-frequency, and land surface parameters without the need for a priori knowledge. Therefore, these models are known as strong tools in estimating *SWE* and can overcome the *SD* retrieval challenges of typical approaches, such as empirical and semi-empirical models. Despite the computational capabilities of ANN, neural network inversion algorithms face a number of challenges, including the training method, NN structure, and training input data. Dependent inputs and inappropriate training methods result in large errors in simulations.

Compared with ANN, the SVM method, which is a well-known model in image classification, better performs in simulating the multi-frequency brightness temperature [148]. In addition, Xiao et al. (2018) [149] showed that the SVM snow-depth algorithm exhibits better performance than the ANN method, the Chang model, the linear regression algorithm, and the spectral polarization difference algorithm, because the saturation effect is alleviated, which makes this model usable for simulating deep snowpack. Similarly, the decision tree (DT) model, which uses if-then rules to classify the information, is preferred compared to ANN due to the extremely rapid calculation process and high estimation accuracy [150]. Random forest (RF), an ensemble classifier, utilizes a set of DTs to prevail over the weakness of a single DT [151]. Since RF does not require uncorrelated inputs, representative variables, and complex mathematics, it is known as a high-speed algorithm.

Markov Chain Monte Carlo (MCMC) is another robust method based on the Bayesian statistical theory, which is able to synergize the retrieval by the simultaneous use of active and passive remote sensing or multiple frequencies. The Bayesian Algorithm for *SWE* Estimation with passive microwave measurements (BASE-PM) has been developed using the MCMC method to simulate the multi-layered snowpack through brightness temperatures

at four frequencies [34,41]. Due to the smaller number of T_B measurements than that of estimated snow parameters, the algorithm uses some prior information on snow density, grain size, temperature, etc., to reduce the *SWE* retrieval uncertainty. Considering the differences between simulated and observed T_B as well as differences between estimated and prior snow parameters, MCMC can find a combination of estimated snow parameters providing the highest possible posterior probability. Although there is no need for further understanding of the forward models, which are used to take into account the microwave emission theory, the computational cost of the method to achieve a stable posterior *SWE* distribution is high. However, MCMC is still utilized as a powerful tool to assess the possibility of parameter retrieval as well as the accuracy of prior knowledge.

Overall, machine learning algorithms lead to an increase in the *SWE* retrieval accuracy to some extent; nevertheless, they should be used cautiously, as the machine learning approach may behave like a black box without a clear physical basis.

Data Assimilation Methods

Data Assimilation (DA) techniques help to modify the overall representation of a system by merging the observation into snowpack models [152–156]. One of the key advantages of the DA technique is that the uncertainty of output is lower than that of observations and models [60]. However, the scale mismatch between the point in situ observations and gridded snow model estimates when combined in assimilation systems is an unavoidable problem, affecting the statistical properties of simulations especially in mixed pixels and complex terrains [61,157]. In addition, the accuracy of the DA approach can be affected by insufficient observing networks and assimilated observations with temporal inconsistency [158,159].

Numerous DA methods, from the simplest structures to more complicated ones, as well as different types of observations, can be exploited to update the snow depth and *SWE* estimates. Basic approaches employ a simple, direct insertion method [160–162] or Cressman interpolation [163–165] to assimilate the observation and update the snow water equivalent. In the direct insertion method, the model parameters are directly replaced with observations, and other non-observed variables are adjusted by the model integration. Cressman interpolation also is a simplified DA method and corrects the parameter sets using observations weighted by the distance to the points. Other approaches, such as optimal interpolation schemes [166–170], consider the observational uncertainty [171]. The optimal interpolation is centered on the Best Linear Unbiased Estimate (BLUE [172]) and is used only for simple, linear models with Gaussian errors. Therefore, the method fails in complex, non-linear snow structures. In this regard, the bias-detecting-ensemble (BDE) is applied to dynamically combine snow-related observations with the models with any complexity [173]. In addition, BDE is capable of improving the results at unobserved sites, illustrating its strength in describing spatial variations. It should be noted that the model, unlike optimal interpolations, does not consider observational uncertainties.

As a popular DA method, filtering systems use a sequential process, which is based on past and present observations fixed in time, to implement the forecast and analysis steps, respectively. The first filter version is the Kalman Filter (KF) [174], which is based on the least-squares analysis to evaluate the assimilation of snow parameters through observations. Due to the linearity assumption of the KF, the method is used for linear models with Gaussian errors. To simulate non-linear structures, the Extended Kalman Filter (EKF) can be applied based on the local linearization of the operators [175–177]. Furthermore, the Ensemble Kalman Filter (EnKF; [178]), which obtains a parameter estimate and its uncertainty with an ensemble, provides a much more convenient execution for non-linear models. The method is able to deal with large dimension error covariance matrices, and propagates the error information by using Monte Carlo sampling [179,180]. However, the EnKF performs poorly in highly non-linear systems and has a high computational cost for larger ensembles. EnKF and EKF have often been utilized for the assimilation of PMW-based *SWE* products, such as SMMR and AMSR-E [17,150,154,181]. To address the non-linearity

issues, the ensemble-based Particle Filter (PF), which produces the probability density function (PDF) by an ensemble of results to consider the dynamics of non-linear systems, is the most suitable DA method. The PF method, similar to the EnKF, represents a sequential Monte Carlo simulation and considers the uncertainties of model structure, forcing data, and observations [153,182,183]. However, the PF determines the uncertainties of state variables more accurately than the EnKF method using state variables resampling [184]. Unlike the other DA methods, the PF can overcome the variable dimension problem, yet the resampling in models with numerous variables leads to very close particles and thereby degeneracy.

Another type of DA method is the smoother approach, which uses a batch of observations over a retrospective window instead of updating the parameters and predicting forward. Smoothers provide a practical approach to obtaining the historical reanalysis datasets for seasonal snow processes (e.g., [185,186]). Compared to filters, smoother methods can extract more information when the seasonal relationships between state variables and observations are strong. Fixed-interval smoothing is the most popular method of this approach in which the variable in a time interval is obtained from assimilating observations of the same interval. A batch smoother, known as the four-dimensional variational method (4DVar), assimilates the measurements of prior knowledge, errors, and model constraints, using minimization of the least squares cost function. Although 4DVar can be used in non-linear models, its application is restricted in complex non-linear models (most snowpack models) due to a need for the adjunct model. The Particle Batch Smoother (PBS), the Ensemble Kalman Batch Smoother (EnBS), and the Ensemble Kalman Smoother (EnKS) developed based on the filtering approaches are other smoother methods. Compared to the EnKS in which a Kalman is updated on all states, particles of the PBS are updated by performing conditioning on all measurements. The batch EnKS is a straightforward method with the same limitations as the EnKF; however, its application is limited by primary additional cost, while the PBS method, similar to the PF, is more cost-effective because of updating ensemble weights instead of state vectors [187], and is applicable for both non-Gaussianity and non-linearities. In addition, Li et al. (2017) [188] demonstrated that the EnBS performed better than the EnKF and EnKS as it partly overcomes the saturation of T_B in deep snowpack due to using T_B time series. It is worth noting that smoothers, due to their retrospective nature, are suitable for deriving the reanalysis data.

In addition to different DA methods used, various types of observations can be assimilated to improve the estimation accuracy of snow water equivalent. The in situ snow water equivalent and snow depth data are the prevalent datasets that can be applied to the snow models to improve the accuracy of *SWE* estimates [169,189,190]. Although it is proven that the use of in situ snow depth improves the accuracy of *SWE* and snow density simulations [191], an extremely dense network of in situ observations is needed to recover the spatial variations of snow properties [173]. The information extrapolated to cells without observations, in turn, leads to uncertainty in *SWE* retrievals as a result of the limited station network. Therefore, remotely sensed information is usually required to be combined with in situ observations, especially on complex surfaces [192]. For example, Hedrick et al. (2018) [193] integrated the LIDAR-derived snow depth into a snow model by direct insertion to improve the estimation accuracy of snow depth at a high resolution. Similarly, Margulis et al. (2019a) [194] assimilated the LIDAR snow depths into a snow cover model via the PBS in order to estimate *SWE*. Andreadis and Lettenmaier (2006) [152] used the AMSR-E *SWE* product to improve the *SWE* estimates, but the assimilation led to a decrease in model accuracy due to the weak performance of the AMSR-E in simulating deep snowpack. The GlobSnow *SWE* product [42] also assimilates the ground-based snow depth data using a Bayesian approach under the observation operator of the HUT model.

Due to avoiding the propagation of data biases in the DA system, low-level satellite data such as radiance provide another powerful dataset to improve *SWE* estimation. However, several points should be kept in mind when assimilating such data, including the prior knowledge requirement with respect to snow structure, complexity in partial snowy surfaces with exposed vegetation, and high nonlinearity of such an assimilation system,

which is more suitable for particle filters and batch smoothers compared to the extent of the EnKF. Kim et al. (2019) [195], who used a particle filter approach, demonstrated that the use of airborne observations of multi-frequency passive radiance with high resolution can improve *SWE* accuracy, while the merger of these observations with a three-layer snow model through the Kalman Filter caused a lower accuracy for *SWE* outcomes [60].

The most widely used source of information for *SWE* estimation is snow cover area (or fraction) [196]. Because of the binary nature of the snow cover area information, an observation operator should be defined for the physically based snow model without violating the physics. Despite this challenge, *SWE* reanalysis by snow cover area (or fraction) data through smoothers has had major success. In this way, a large number of studies have estimated the *SWE* reanalysis data over a long period by combining snow cover area (or fraction) with batch smoothers (e.g., [72,185,186,197]). In addition, Andreadis and Lettenmaier (2006) [152] exerted the MODIS snow cover area observations to update the *SWE* obtained from the VIC model using the EnKF method.

Other snow-related data such as spatially extensive albedo can map the snow water equivalent by being combined with the land surface models and snowpack modules. For instance, Painter et al. (2016) [198] merged the airborne albedo maps with a snow model to simulate the snow density and, thereby, the *SWE* spatial distribution in mountain areas. Piazzi et al. (2018) [171] assimilated various snow-related data, including snow temperature, albedo, snow depth, and *SWE* for offline simulations. Durand and Margulis (2006) [199] tried to assimilate albedo and the brightness temperature obtained from the AMSR-E and SSM/I into the simple snow-atmosphere-soil transfer (SAST) model in order to improve the accuracy of *SWE* retrievals. In addition, some studies used the direct insertion method to assimilate albedo maps and obtained improved simulations for *SWE* and snow depth [146,162].

Effective Criteria in DA Method Selection

Several criteria determine the appropriateness of the DA method, explained as follows:

- The characteristics of assimilated observations

The spatial representation of observed data, including lumped and distributed representations, affects the DA process. In addition, the similarity of observation data with the objective parameter or variable is another factor; it is required to convert the observations to the model variables if the variable is not directly observed.

- The complexity level of snowpack models

The snow models with multiple layers are problematic to update with bulk observations. This issue is also challenging for models with multiple state variables (such as snow temperature, snow density, and liquid water content), as the variables are usually not observed and have a weak correlation with observed states. Generally, the complexity of assimilation schemes increases with increasing the spatial resolution of the model and the prediction time period [200].

- The ability of the DA method in forecasting and propagating

The application of DA methods in predicting forward, such as *SWE* reanalysis, is another reason to choose the method. Moreover, in the spatial propagation of analysis, the ability to predict non-observed pixels affects the choice of the DA method. It should be noted that the question of how to propagate requires more assessment as an ongoing research area.

4.3. Active Microwave

Despite the capability of the passive microwave remote sensing in monitoring the snow parameters continuously, the factors of coarse spatial resolution, exclusion of mountain areas, and requirement of bias correction in deep snowpack cause inefficiency of this method on the small spatial scales. In contrast, the active microwave remote sensing can

provide *SWE* information at a fine spatial resolution, which makes it appropriate for local applications. However, the active microwave suffers from a lack of physical concept in estimating *SWE* [38].

The X and C band data obtained from Space-Borne Imaging Radar-C and X-band Synthetic Aperture Radar (SIR-C/X-SAR) were the earliest efforts made to achieve snow parameters [201,202]. Over time, a large number of data, with different polarizations, frequencies, and incidence angles, have been retrieved by Synthetic Aperture Radar (SAR) sensors, such as the Huan Jing (HJ), Gaofen (GF), Earth Resources Satellite (ERS), RADARSAT, Environmental Satellite Advanced Synthetic Aperture Radar (Envisat ASAR), Terra SAR-X, and Phased Array type L-band SAR (PALSAR). The SAR system measuring the backscatter, the signal received by the sensor, estimates the snow parameters by increasing the volume scattering proportional to the snow mass. The vertical heterogeneity caused by structural variations of snow affects the backscatter and, thereby, *SWE*.

In order to obtain the snow parameters, two types of inversion algorithms using active remote sensing are generally used. The first group is based on the physical backscattering achieved from the responses of scattering intensity compositions to different polarizations and frequencies. The total backscattering intensity, composed of surface and volume scattering, estimates the snow parameters such as *SWE* by inverting the SAR measurements. It should be noted that the X and Ku band data are more effective to calculate *SWE* because of their high sensitivity to snow. On the other hand, the algorithms of the second group are based on the interference SAR measurements and estimate *SWE* by the phase shift of radar waves. Therefore, this type of inversion model is appropriate for data with low frequencies (long wavelengths), such as C and L band data.

4.3.1. *SWE* Inversion Techniques Based on the Physical Backscattering

Radar backscattering coefficients at the incidence angle θ are calculated by the following general equation:

$$\sigma_{pq}^t(f') = \sigma_{pq}^s(f') + \sigma_{pq}^v(f') + \sigma_{pq}^i(f') + L'_p L'_q T'_p T'_q \sigma_{pq}^g(f') \tag{32}$$

where σ_{pq}^t is the total radar backscatter at polarization pq, and f' is frequency. The superscript s indicates surface backscattering of the air–snow and snow–soil interfaces, the superscript v represents the volume scattering of the snowpack, and the superscript i shows the interaction between the underlying soil and snowpack. L' is the snowpack attenuation coefficient, T' is the power transmission coefficient at the air–snow interface, and σ_{pq}^g is the scattering coefficient directly originating from soil. The estimation accuracy of scattering components depends on snowpack characteristics, polarization, radar frequency, and incident angle. Different assumptions are considered to represent the response of microwave radiation to snowpack structure, including the random medium of ice and air, bicontinuous medium approach, collections of individual snow spheres, sticky hard spheres, and the empirical relationship between grain size and scattering coefficient.

Empirical models [78,203], multiple channel measurements [201,204], and the RTE-based physical models [205–208] are also used to determine the snow parameters. RTE-based physical models include the estimation of prior parameters, the modeling of snow volume scattering, and a cost-function inversion to calculate *SWE*. According to the RTE, the volume scattering depends on the snow depth, microstructure, density, and stratigraphy [204,208,209]. Given that the different combinations of snow parameters can generate the similar backscatter [209], the prior estimation can improve the retrieval accuracy by constraining the cost function.

A relationship between snow optical thickness, single scattering albedo, and snow volume backscattering is established to estimate *SWE* by a parameterized scheme in which

a cost function is iteratively minimized [140]. This cost function, defined as the difference between the observed and estimated signals, is shown by Equation (33):

$$F = \sum_{i=1}^{4} \frac{\left[\sigma_i^{obs} - \sigma_i^{est}(x_1, x_2)\right]^2}{2v_i^2} + \sum_{i=1}^{2} \frac{[x_i - \overline{x}_i]^2}{2vp_i^2} \tag{33}$$

where i is the number of channel (equal to 4 for VH and VV polarizations of Ku and X bands), σ_i^{obs} and σ_i^{est} are the observed and estimated backscattering signals, respectively, x_i indicates the snow microstructure (i.e., optical thickness and single scattering albedo), $\overline{x}_i$ denotes the mean of x_i, v is the error variance of radar measurements, and vp is the variance of a priori constraint. It should be noted that the term $\frac{[x_i - \overline{x}_i]^2}{2vp_i^2}$ shows the prior estimation in which optical thickness is the most important parameter. The absorption component of snow optical thickness (τ_a) is related to the snow depth by Equation (34):

$$\tau_a(f') = \mathbb{k}_a(f') \times SD \tag{34}$$

where $\tau_a(f')$ shows the absorption part of optical thickness at frequency f', $\mathbb{k}_a$ is the snow absorption coefficient, and SD is the snow depth. In addition, $\mathbb{k}_a$ is obtained from Equation (35) as below:

$$\mathbb{k}_a = V_s k_0 \frac{\acute{\varepsilon}}{\varepsilon} \left| \frac{3\varepsilon}{\varepsilon_i + 2\varepsilon} \right|^2 \tag{35}$$

where V_s is the volume fraction of snow, k_0 is the SAR wave number, ε is the dielectric constant, and $\acute{\varepsilon}$ is the imaginary part of ε. Finally, SWE is achieved from the following equation:

$$SWE = \tau_a(f') \frac{0.917}{0.33 k_0 \acute{\varepsilon}(f')} \tag{36}$$

The SAR bands, along with their frequencies and wavelengths, are shown in Table 1. The Ku band is more sensitive to snow properties, and most snow volume signals are formed at this band [210]. Generally, the bands with high frequency are more applicable for snow characterization because of their high sensitivity [211,212]. For example, the contribution of X band signals from a snowpack is more than that of the C band, i.e., approximately 60% versus 30%. Therefore, the X band is much more sensitive to snowpack, which makes it more reliable in inverting the snow parameters. In addition to the typical snowpack, the radar frequencies should be capable of penetrating a thick snowpack, and a strong snow scattering signal is needed for inversion. Accordingly, the Ku and X are considered the most optimal bands for snow observing. The Ka band, which has the shortest wavelength, cannot provide sufficient penetration into the snowpack because the signals at this band are weakened by the shape and grain size of the snowpack. On the other hand, the bands with longer wavelengths, such as C and L bands, are mainly affected by the underlying ground surface characteristics; therefore, the snow depth estimation using these bands requires elimination of the ground backscattering [20].

The satellite mission Cold Regions Hydrology High-Resolution Observatory (CoReH2O) [204] was designed to fill the gaps available in snow detection by X and Ku bands. In addition, the Water Cycle Observation Mission (WCOM) [213] with combined passive and active microwave sensors was proposed to monitor SWE. Similar to the configuration of CoReH2O, a dual-frequency polarized scatterometer with Ku and X bands has been planned to improve global coverage due to its spatial resolution (2~5 km).

4.3.2. *SWE* Inversion Techniques Based on the SAR Signal Phase

The inversion algorithms based on radar backscattering use the concepts of microwave scattering and require the complex physical models. As another promising approach, the use of signal phase can provide the additional data about the snow properties. Techniques of ultra-wideband radar, tomography, and interferometry employ this approach, described below.

Table 1. The properties of SAR bands.

Band	Frequency (GHz)	Wavelength (cm)
Ka	27–40	0.75–1.1
K	18–27	1.1–1.67
Ku	12–18	1.67–2.4
X	8–12	2.4–3.75
C	4–8	3.75–7.5
S	2–4	7.5–15
L	1–2	15–30
P	0.3–1	30–100
UHF	0.03–0.3	100–1000
VHF	0.003–0.03	1000–10,000

Ultra-Wideband Radar

Ultra-wideband radar, which uses extremely short pulses to obtain a very wide bandwidth, can monitor reflections from different depths of snowpack layers. This method is capable of estimating the snow depth-dependent refractive index as well as the major parts of the snowpack in backscattering generation, which leads to the indirect determination of *SWE* and snow depth. However, the ultra-wideband radar technology, because of the limitations of bandwidth and frequency allocation, is not usable from the space. The L band GPR systems [214,215], multi-channel L-band radar [216], Nadir ultra-wideband FM-CW radar [217,218], and airborne FM-CW experiments [219] are some examples using this method.

Tomography

The SAR Tomography (TomoSAR) monitors the snowpack using frequencies X to Ku bands [220]. The TomoSAR technique with polarimetric capabilities can partition the signals into the surface and volumetric scattering components, distinguish between canopy, soil, and snow, and detect different types of sizes and shapes. In addition, this method is capable of separating multiple snow layers and identifying density changes, which leads to an improvement in *SWE* retrieval.

Interferometry

Interferometry determines the differential path length and electromagnetic path length of snow signals. The interferometric response can change with polarization, wavelength, the scattering properties of the snowpack, and the snow–soil and snow–air interfaces [221,222]. The interferometry method is carried out between two observations in space as well as repetitive observations. The repeat-pass SAR interferometric measurements directly estimate *SWE* and its relative changes through phase shift caused by snowpack [223]. This method is used for low-frequency measurements at C and L bands while the radar backscattering at these bands is weakened by scattering from the soil–snow interface. The repeat-pass interferometric phase φ is characterized by the equation below:

$$\varphi = \varphi_{flat} + \varphi_{topo} + \varphi_{atm} + \varphi_{noise} + \varphi_{snow} \tag{37}$$

where φ_{flat} and φ_{topo} are the phase differences caused by changes in the distance between the target and satellite in flat and complex terrains, φ_{atm} is due to the variations of atmospheric propagation, φ_{noise} is the phase noise, and φ_{snow} indicates the two-way propagation difference in snow relative to the air, which is obtained as below [223]:

$$\varphi_{snow} = -2k_i SD(\cos\theta_i - \sqrt{\varepsilon - (\sin\theta_i)^2}) \tag{38}$$

where k_i indicates the incoming radar beam vector, SD is the snow depth, θ_i is the incidence angle, and ε is the dielectric constant of snow. For an incidence angle of $23°$, the phase difference caused by changes in SWE is obtained from a linear relationship as follows [223]:

$$\varphi_{snow} = -2k_i 0.87 \Delta SWE \tag{39}$$

In surfaces with wet snow, the elevation difference of snowy and snow-free surfaces, which can be obtained from the Ka band, is used for the estimation of snow depth [224].

5. *SWE* Products

The generation of an accurate dataset across all snowy regions, because of widely spatial changes in snow properties, requires a physical method to robustly simulate snow-pack [18] or a regional method to statistically parameterize the snowpack processes [81]. The application of the statistical approach is mostly limited to the regions with calibrated retrieval schemes while the physical approach, unlike its challenging implementation, has widely applicable potential. Generally, available SWE products are classified into three main groups, including satellite, reanalysis, and data assimilation datasets, explained as follows and summarized in Table 2.

5.1. Satellite SWE Products

The satellite SWE datasets are based on the brightness temperature observations retrieved from the passive microwave data without any ancillary data. Most SWE algorithms employed by space-borne observers use the combination of channels with 37 (sensitive to scattering by snow) and 19 (low-sensitive to scattering by snow) GHz. The difference of T_B at these channels, with the benefit of reducing the physical temperature effect on measured brightness temperature relative to single-frequency analysis, shows the SWE value [79]. Furthermore, both vertically (V) and horizontally (H) polarized channels can be used to retrieve SWE with similar results; however, V-based channels are preferred due to less sensitivity to snow layering [225]. The SWE variable detected using space-borne sensors has acceptable accuracy over regions with consistent snow properties and insignificant altitudinal and vegetation variability. The most common satellite-based SWE products are listed as follows:

The *Advanced Microwave Scanning Radiometer for Earth Observing System* (AMSR-E; [226]) is a microwave radiometer onboard the Aqua satellite with microwave frequencies of 6.9, 10.7, 18.7, 23.8, 36.5, and 89 GHz in vertical and horizontal polarization. AMSR-E produces global SWE observations based on the algorithm introduced by Chang et al. (1987) [30] and amended by Kelly et al. (2003) [82]. This product distinguishes the shallow and non-shallow dry snowpack by brightness temperature thresholds [82] and estimates SWE using the brightness temperature difference at two frequencies: 19 and 37 GHz [227]. In addition to considering the snow grain size variations, the AMSR-E product uses the 10.7 GHz frequency to take into account the vegetation influence for deeper snow. The snow density from [228] and [229] and snow climate classification from [230] are used to convert the snow depth to SWE.

The Scanning Multichannel Microwave Radiometer (SMMR; [231]) is a microwave instrument onboard NIMBUS-7 with frequencies of 6.6, 10.7, 18, 21, and 37 GHz in both vertical and horizontal polarization [83]. The microwave frequencies for SWE retrieval are 18 and 37 GHz [79].

The *Special Sensor Microwave/Imager* (SSM/I; [232]) is an instrument onboard the DMSP F-series satellites with microwave frequencies of 19, 22, 37, and 85 GHz. All channels, except 22 GHz, which has only vertical polarization, include both vertical and horizontal polarization [83]. In addition, the 19 and 37 GHz frequencies are employed to estimate SWE data.

The *Advanced Microwave Scanning Radiometer 2* (AMSR2; [226]) is a remote sensing instrument onboard the GCOM-W1 satellite launched by the JAXA, and produces global SWE estimates by measuring weak microwave emission.

The *Advanced Microwave Sounding Unit* (AMSU; [77]) is a microwave radiometer onboard the National Oceanic and Atmospheric Administration (NOAA) Polar Operational Environmental Satellites (POES), and has two modules: AMSU-A and AMSU-B, with the nadir resolutions of 48 km and 16 km, respectively. *SWE* retrieval is based on an empirical relationship that uses brightness temperature measurements at 23, 31, and 89 GHz channels. Despite the coarse spatial resolution, AMSU has larger spatial coverage and more additional channels in comparison with AMSR-E and SSM/I, which makes the *SWE* estimates more robust [77].

5.2. Reanalysis SWE Products

In reanalysis products, the best features of observations and models are used to recreate the climate variables field [83]. The most widely used reanalysis *SWE* products are presented below:

The National Centers for Environmental Prediction (NCEP) Climate Forecast System Reanalysis (CFSR; [233]) presents a reanalysis dataset, which is achieved by combining the globally coupled land–atmosphere–ocean–sea ice system and global precipitation analyses obtained from the Climate Prediction Center Unified (CPCU) daily gauge analysis datasets [234] and the Climate Prediction Center (CPC) Merged Analysis of Precipitation (CMAP; [235]). The snowpack simulation is performed by the Noah land surface model [236], and the CFSR snow analysis is based on the Snow Depth model (SNODEP) [237]. The SNODEP assimilates the snow cover area obtained from the National Environmental Satellite Data and Information Service (NESDIS), Interactive Multi-sensor Snow and Ice Mapping System (IMS; [238]), and in situ observations to produce a global snow depth analysis through the detection algorithm of the SSM/I. The SNODEP model has low accuracy in estimating *SWE* due to the sparse in situ measurements [239]. It should be noted that a 10:1 ratio is utilized to convert the snow depth data to *SWE*.

ERA40 [240] is a common reanalysis product from the European Centre for Medium-Range Weather Forecasting (ECMWF). The data assimilated within ERA40 include observational snow depths and SSM/I brightness temperatures. Reichler and Kim (2008) [241] introduced ERA40 as one of the best available reanalysis products.

ERA-Interim (ERA-I; [165]) is a global reanalysis dataset obtained from the ECMWF. The land component of ERA-I called the Tiled ECMWF Scheme of Surface Exchanges over Land (TESSEL) is driven using the ECMWF with the snow module proposed by Douville et al. (1995) [242]. ERA-I updates the snow analysis based on the assimilated IMS snow cover and the Cressman analysis of snow depth observations [164,243]. According to [244], ERA-I detects the melt season for forested areas too early and also underpredicts snowfall values. Moreover, Kapnick and Delworth (2013) [245] reported a negative bias for ERA-Interim *SWE* in coastal areas and a snow underestimation for locations with midlatitude.

ERA-Interim/Land (ERA-I/L; [246]) is another reanalysis dataset achieved from the ECMWF. The land component of the ERA-I/L is based on the offline Hydrology Tiled ECMWF Scheme of Surface Exchanges over Land (HTESSEL) model, which is a revised version of TESSEL with a simple, single layer snowpack module developed by Dutra et al. (2010) [244]. The forcing data include the ERA-Interim atmospheric dataset and precipitation modified using the Global Precipitation Climatology Project (GPCP; [247]). The ERA-I/L, unlike the ERA-I, does not assimilate any station-based snow data into the model.

ERA5, the ECMWF Reanalysis version 5, is similar to ERA-I/L in terms of its land component and snowpack module. The dataset updates the snow reanalysis using a two-dimensional optimal interpolation of in situ snow depth and IMS snow cover.

ERA5-Land [248] is the improved version of ERA5, which provides global snow data, including snow cover, albedo, density, temperature, depth, snowfall, snowmelt, and *SWE* from 1981 onwards.

Crocus [249] has been obtained from the Interactions between Soil, Biosphere, and Atmosphere (ISBA) land surface model forced by ERA-Interim meteorological data. The

snowpack module of the dataset is the Crocus snow scheme, which is a complex physically based snowpack model with multiple snow layers representing distinct snowfall events. Each snow layer is identified by the liquid water content, density, temperature, thickness, and grain properties.

Japanese 55-year Reanalysis (JRA-55; [250]) simulates the land component based on the offline SiB model [251] driven by precipitation that is revised using precipitable water (PW), which is obtained from the SSM/I brightness temperature [252]. The snow analysis is carried out based on the two-dimensional optimal interpolation of observed snow depth and snow cover data retrieved from the Special Sensor Microwave Imager/Sounder (SSMIS) and SSM/I. It should be noted that the SiB uses the maximum depth between 2 cm and the climatological depth to simulate ice sheets due to the lack of the physical processes for ice sheets within the SiB model.

Modern-Era Retrospective Analysis for Research and Applications (MERRA; [253,254]) is a global reanalysis product that assimilates NASA's EOS satellite observations into a climate model [253]. The land component of the dataset is simulated using the Catchment model [255] driven by precipitation that is modified based on the CPCU and CMAP data, similar to the CFSR. The snow scheme of the model has an intermediate complexity with up to three snow layers, in which the processes of snow accumulation, melting, compaction, and refreezing are simulated without any snow data assimilation [256]. The snow depth data derived from MERRA showed a bias of 21.0 cm and a correlation of 0.56 in comparison with in situ observations of the World Meteorological Organization (WMO). By rerunning the land surface component with atmospheric data of the MERRA product, except for precipitation that is obtained from NOAA's CPCU dataset, the MERRA-Land model has been produced.

5.3. Data Assimilation-Based SWE Products

Examples of DA-based products, which estimate *SWE* data by combining the land surface models and snow modules with different types of observations, are listed below:

The *Global Land Data Assimilation System* (GLDAS; [160]) provides a DA-based dataset using the different forcing data and land surface models. The first version of GLDAS uses the NOAA Global Data Assimilation System (GDAS) with precipitation obtained from the CPC CMAP, while the GLDAS version 2 is forced by the Global Meteorological Forcing Dataset from Princeton University. On the other hand, the land surface models used to estimate *SWE* include the VIC land surface model [257]; the Mosaic land surface model [258], the Community Land Model (CLM) [259], and the Noah land surface model. The structure of snowpack modules implemented in land surface models varies from simple single-layer structures (in the Mosaic and Noah models) to intermediate complex structures (in VIC and CLM). It is worth noting that no snow data assimilation is carried out in the GLDAS dataset.

The *North American Land Data Assimilation System* (NLDAS; [260–262]) is a DA-based reanalysis product, with forcing data obtained from the North American Regional Reanalysis (NARR) model [263] and in situ precipitation of the CPC adjusted by the Parameter-Elevation Regressions on Independent Slopes Model (PRISM) [264]. Land surface models used within the NLDAS include VIC, Mosaic, and Noah.

Sierra Nevada Snow Reanalysis (SNSR; [185]) is another assimilation-based reanalysis dataset, with input data obtained from the NLDAS dataset. The *SWE* estimates are updated and constrained by the Landsat snow cover fraction data, leading to optimal results. Though the SNSR considers the canopy effect on the snow accumulation and melting processes, the forest cover has no significant effect on the reanalysis algorithm on a watershed scale. According to an extensive validation of the dataset against in situ data, a bias of less than 3 cm, R greater than 0.95, and RMSE less than 13 cm were achieved [185].

The *Canadian Meteorological Centre* (CMC; [168]) is an assimilation-based dataset providing daily snow depth across the Northern Hemisphere through integrating in situ snow depth and model simulations. Using the snow density derived from snow course

measurements, the *SWE* data with a monthly temporal scale are produced. The results mostly depend on the model simulation in regions with few observations, although *SWE* is well-constrained by observational data in areas with a dense network. According to [100], the CMC, in comparison with snow course data, tends to estimate a little snow cover during the summer and begins the snowmelt in the spring too early.

North American Regional Reanalysis (NARR; [263]) is an assimilation-based dataset over North America generated by NCEP. The NARR dataset reaches peak *SWE* nearly three months prior to the Snowpack Telemetry (SNOTEL) data [265]. In addition, it is found that NARR is incapable of indicating an obvious annual cycle for *SWE* so that the melting and accumulation processes occur multiple times throughout the season. In this regard, Salzmann and Mearns (2012) [265] concluded that NARR is more appropriate for snow cover diagnosis than *SWE*, possibly owing to its poor correlation with SNOTEL *SWE*.

The *National Weather Service Snow Data Assimilation System* (SNODAS; [266]) is another assimilation-based dataset, developed by the National Weather Service (NWS), and produces the *SWE* data over the continental United States by merging station data, snow model simulations, and airborne observations. The assimilated data include satellite snow cover, radar precipitation data, airborne gamma radiation, and in situ measurements of snow courses and snow pillows. It has been shown that SNODAS performs well in forest regions, and conversely has a poor performance in alpine areas [267,268]. Furthermore, SNODAS underestimates snow depth for deep snowpacks and dense canopies [268].

Global Snow Monitoring for Climate Research (GlobSnow; [42]) is a global dataset released by the European Space Agency (ESA), which combines satellite-based PMW with ground-based snow depth measurements to quantify *SWE* using Bayesian non-linear iterative assimilation [42,145]. The retrieval scheme is based on the HUT model and vertically polarized observations of brightness temperature at 19 and 37 GHz obtained from the SSM/I, SMMR, and SSMIS instrument on the DMSP [269]. According to [42], the kriged snow depth field is used as the input for the forward microwave emission model to estimate the snow grain size and snow depth in two iterations. The algorithm accounts for the effect of forest transmissivity and snow density variation on the snow depth by the empirical model presented by Kruopis et al. (1999) [270] to refine the brightness temperature. It should be noted that the alpine regions are excluded from the simulation process as the approach is incapable of estimating *SWE* in complex terrains [42]. The comparisons of *SWE* retrievals with airborne or ground-based observations showed that the model is capable of simulating snow water equivalent under various land cover types and snow conditions [271,272]. In addition, the model demonstrated comparable performance with other models driven by ground-based data [101,273], and better performance than other *SWE* products [42]. However, it performs poorly in wet snow as well as deep dry snowpack, due to greater absorption of microwave signals rather than scattering [42,101,145].

Table 2. A summary of available *SWE* datasets.

Product	Retrieval Approach	Snow Scheme	Land Model	Snow Data Assimilation	Temporal Resolution	Spatial Resolution	Time Coverage	Spatial Coverage	Ref
GlobSnow	Assimilation-based	Simple	-	Ground-based SD and PMW signals	Daily; weekly; monthly	25 km	1979-present	Northern Hemisphere	[42]
GLDAS	Assimilation-based	Simple Intermediate	Noah Mosaic VIC CLM	Meteorological data obtained from CPC CMAP and Princeton University	Hourly daily monthly	$1° \times 1°$ $0.25° \times 0.25°$	1979–2020 1948–2014	Global	[161]
ERA-I	Reanalysis	Simple	TESSEL	IMS	Hourly Daily monthly	$0.25° \times 0.25°$	1979–2019	Global	[165]
CMC	Assimilation-based	Simple	-	Meteorological observations	monthly	35 km	1998–2014	Global	[168,274]

Table 2. *Cont.*

Product	Retrieval Approach	Snow Scheme	Land Model	Snow Data Assimilation	Temporal Resolution	Spatial Resolution	Time Coverage	Spatial Coverage	Ref
SNSR	Assimilation-based	-	A land surface model (LSM) with a snow depletion curve	Landsat snow cover fraction	Daily	90 m	1985–2015	Sierra Nevada (United States)	[185]
AMSR-E	PMW	-	-	-	Daily	25 km	2002–2011	Global	[226]
AMSR2	PMW + in situ	-	-	-	Daily	25 km	2012-present	Global	[226]
SMMR	PMW	-	-	-	2-days	25 km	1978–1987	Global	[231]
SSM/I	PMW	-	-	-	Daily	25 km	1987–2009	Global	[232]
CFSR	Reanalysis	Simple	Noah	SNODEP, IMS	Hourly-monthly	$0.5° \times 0.5°$	1979–2010; Version 2 updates from 2011	Global	[233]
ERA40	Reanalysis	Simple	TESSEL	satellite radiance data	Hourly Daily monthly	$2.5° \times 2.5°$	1957–2002	Global	[240]
ERA-I/L	Reanalysis	Simple	HTESSEL	-	Hourly	$0.25° \times 0.25°$	1979–2010	Global	[246]
ERA5-Land	Reanalysis	Simple	HTESSEL	-	Hourly monthly	$0.1° \times 0.1°$	1981-present	Global	[248]
Crocus	Reanalysis	Complex	ISBA	-	Daily	$1° \times 1°$	1979–2016		[249]
JRA-55	Reanalysis	Complex	SiB	Satellite radiance data	Hourly daily	$1.25° \times 1.25°$	1957-present	Global	[250]
MERRA	Reanalysis	Intermediate	Catchment	-	Hourly daily monthly	$0.5° \times 0.67°$	1979–2016	Global	[253]
MERRA-Land	Reanalysis	Intermediate	Catchment	-	Hourly daily monthly	$0.5° \times 0.625°$	1979–2016	Global	[254]
NLDAS	Assimilation-based	Intermediate	VIC Mosaic Noah	Terrestrial precipitation, space-based radiation data, and numerical model output	Hourly monthly	12.5 km	1979-present	central North America	[260]
NARR	Assimilation-based	Complex	NCEP Eta Model	Observed precipitation	Hourly daily monthly	32 km	1979-present	North America	[263]
SNODAS	Assimilation-based	Complex	Rapid Update Cycle numerical weather prediction model	Satellite, airborne, and ground-based snow observations	Daily	1 km	2003-present	Continental US	[266]
ERA5	Reanalysis	Simple	HTESSEL	-	Hourly monthly	$0.25° \times 0.25°$	1979 to present	Global	[275]

6. Conclusions and Future Perspectives

An accurate estimation of spatial and temporal changes in *SWE* is one of the most significant challenges of snow hydrology. Due to the high spatial heterogeneity of snow properties, the limited ground-based measurements are incapable of representing *SWE* over large terrestrial extents. Therefore, reconstruction and remote sensing techniques are counted as effective tools used to estimate snow parameters at different scales.

In the reconstruction approach, a backward melt calculation is used to reconstruct *SWE* accumulated from the date t back to the last significant snowfall. The method is applicable if the information of snow cover area and snowmelt rate are known; therefore, the accuracy of the *SWE* results increases with improving SCA and snowmelt measurements. The sensitivity of the method to the SCA data, snowmelt estimation methods, and dates of snow disappearance and peak *SWE* has led to the popularity of remote sensing observations in detecting the snow parameters. In this regard, passive microwave, which uses brightness temperature difference at two frequencies, monitors the global information of *SWE* and snow depth. The attenuation of emitted radiation is related to the scattering and absorption properties of the surface, which are detected using multi-frequency microwave emissions. Various snow inversion models are used to conceptualize the passive microwave brightness temperature, including the empirical approach, statistical approach, and emission models. The empirical models estimate *SWE* based on the brightness temperature differences at different frequencies and can employ both constant and varying snow properties. In

addition to the empirical approach, *SWE* can be derived by a physically based statistical scheme using a regression relationship with the attenuation properties and snowpack radiation. The most well-known approach to parameterizing the microwave interactions is snow emission models composed of three major concepts: (i) snow microstructure parameterization, (ii) solution of RTE, and (iii) snow emission or scattering estimation. Accordingly, three types of models, including semi-empirical models, analytical models, and numerical models, have been formed to estimate snow scattering effects. Although semi-empirical models based on the field measurements benefit a simple structure and low electromagnetic computations, they are limited to small-scale areas. The analytical models use Maxwell's equations instead of traditional radiative transfer theory to model snow microwave emission. These models have a higher accuracy as well as a more complex structure than the semi-empirical models. In comparison with semi-empirical and analytical structures, numerical models are more complicated because of real assumptions, which lead to more realistic snow simulations.

Despite the popularity of passive microwaves in retrieving *SWE*, factors such as coarse spatial resolution, the saturation effect of the signal, the effect of forest attenuation, and the mixed pixel problem cause the complex estimation of *SWE* due to nonlinear relationships between PMW brightness temperature and snow parameters. Therefore, several techniques including iterative algorithms, lookup table algorithms, machine learning, and data assimilation methods are used to improve *SWE* estimation accuracy and implementation of complex nonlinear relationships. Iterative algorithms, which are the basis of emission models, use a forward structure to adjust *SWE* by minimizing the cost function between the observed and simulated brightness temperature. In contrast, a lookup table provides a database of snow parameters to estimate *SWE* by seeking brightness temperature combinations similar to observed ones. To parameterize the complex relationships between PMW signals and snow parameters, nonlinear machine learning techniques such as ANNs, SVMs, and RFs are counted as strong tools. However, inappropriate training methods and dependent input data can cause large errors in simulations. On the other hand, the statistical combination of satellite data and in situ observations made by the data assimilation technique can alleviate the mixed pixel issue, especially over the areas with forested coverage. Although the DA approach can improve the accuracy of output in comparison with observations and model simulations, the scale mismatch between the point and gridded data affects the statistical indices of results. In addition to DA technique, active microwave remote sensing combined with providing the *SWE* information at a fine resolution overcomes the coarse spatial resolution of passive microwave, which makes it appropriate for local applications. Two types of inversion algorithms estimate snow depth by using active remote sensing, including physical backscattering algorithms and phase-based algorithms. The models based on physical backscattering simulate the snow properties by concepts of microwave scattering via complex physical structures. Phase-based algorithms, however, provide a simpler way to retrieve the *SWE* by using techniques of ultra-wideband radar, tomography, and interferometry.

Finally, a method (or dataset) that is capable of accurately estimating snow-related characteristics across all snowy regions is challenging yet useful. Currently, most PMW-based algorithms estimate *SWE* based on the semi-empirical approaches, which require validation in regions with different conditions. In addition, the canopy covers as well as other types of land covers, due to their effect on the *SWE* estimation accuracy, should be considered to address the mixed pixel problem. In mountainous areas, the impact of surface topography leads to an increase in effective radiation emitted from the surface due to cross-radiation. Therefore, the effect of terrain should be included in inversion algorithms; however, because of its coarse spatial resolution, the PMW is incapable of it. Frameworks coupling land surface models and emission models as well as the frameworks combining emission models and ground-based observations by using assimilation methods can compensate for the coarse spatial resolution of PMW. In this regard, developing a systematic method that can generalize the snow properties from a small scale to a global

scale is an open question that should be assessed more. The long-term field observations can be a promising solution for evaluating this question further. On the other hand, although active remote sensing can address the issue of PMW spatial scale by observing the features at higher resolution, the frequencies used by space-borne radar systems (X and Ku bands) are not sensitive to dry snowpack. Therefore, the development of algorithms using high-frequency radar observations is an important issue for active microwaves in the future.

Abbreviations

Acronyms

SWE	Snow water equivalent
SCA	Snow cover area
NIR	Near infrared
VIS	Visible spectral
PMW	Passive microwave
SMMR	Scanning multi-channel microwave radiometer
SSM/I	Special sensor microwave/imager
DMSP	Defense Meteorological Satellite Program
AMSR-E	Advanced Microwave Scanning Radiometer for Earth Observing System
AMSR2	Advanced Microwave Scanning Radiometer 2
EOS	Earth Observing System
JAXA	Japan Aerospace Exploration Agency
GCOM-W1	Global Change Observation Mission 1st-Water
AMSU	Advanced Microwave Sounding Unit
NOAA	National Oceanic and Atmospheric Administration
POES	Polar Operational Environmental Satellites
RTE	Radiative transfer equation
LSM	Land surface model
IDW	Inverse-distance weighting
MODIS	Moderate-Resolution Imaging Spectroradiometer
TGI	Temperature gradient index
BATS	Biosphere-Atmosphere Transfer Scheme
VIC	Variable Infiltration Capacity
SiB	Simple Biosphere Model
DMRT	Dense Medium Radiative Transfer
AIEM	Advanced integral equation model
SFT	Strong fluctuation theory
RT	Radiative transfer
MEMLS	Microwave Emission Model of Multi-Layer Snow
HUT	Helsinki University of Technology
IBA	Improved Born Approximation
DMRT-ML	DMRT multilayer
QCA	Quasicrystalline Approximation
QCA-CP	Quasicrystalline Approximation with coherent potential

DMRT-QCA	Dense Medium Radiative Transfer with Quasicrystalline Approximation
DMRT-QCA-CP	Dense Medium Radiative Transfer with Quasicrystalline Approximation with Coherent Potential
DMRT-QMS	Dense Media Radiative Transfer with Quasicrystalline Approximation (QCA) Mie Scattering of Sticky spheres
DMRT-AIEM-MD	Dense Media Radiative Transfer with Advanced Integral Equation Model with Matrix Doubling
EFA	Effective field approximation
GRF	Gaussian random field
DDA	Discrete dipole approximation
ANN	Artificial neural network
SVM	Supported vector machine
RF	Random forest
BP	Back propagation
SD	Snow depth
NN	Neural network
DT	Decision tree
MCMC	Markov Chain Monte Carlo
BASE-PM	Bayesian Algorithm for *SWE* Estimation with passive microwave measurements
DA	Data Assimilation
BLUE	Best Linear Unbiased Estimate
BDE	Bias-detecting ensemble
KF	Kalman Filter
EKF	Extended Kalman Filter
EnKF	Ensemble Kalman Filter
PF	Particle Filter
PDF	Probability density function
4DVar	Four-dimensional variational method
PBS	Particle Batch Smoother
EnBS	Ensemble Kalman Batch Smoother
EnKS	Ensemble Kalman Smoother
SAST	Snow-atmosphere-soil transfer
SIR-C/X-SAR	Space-borne Imaging Radar-C and X-band Synthetic Aperture Radar
SAR	Synthetic Aperture Radar
HJ	Huan Jing
GF	Gaofen
ERS	Earth Resources Satellite
Envisat ASAR	Environmental Satellite Advanced Synthetic Aperture Radar
PALSAR	Phased Array type L-band SAR
CoReH2O	Cold Regions Hydrology High-Resolution Observatory
WCOM	Water Cycle Observation Mission
TomoSAR	SAR Tomography
NCEP	National Centers for Environmental Prediction
CFSR	Climate Forecast System Reanalysis
CPCU	Climate Prediction Center Unified
CPC	Climate Prediction Center
CMAP	CPC Merged Analysis of Precipitation
SNODEP	Snow Depth model
NESDIS	National Environmental Satellite Data and Information Service
IMS	Interactive Multi-sensor Snow and Ice Mapping System
ECMWF	European Centre for Medium-Range Weather Forecasting
ERA-I	ERA-Interim
TESSEL	Tiled ECMWF Scheme of Surface Exchanges over Land
ERA-I/L	ERA-Interim/Land
HTESSEL	Hydrology Tiled ECMWF Scheme of Surface Exchanges over Land
GPCP	Global Precipitation Climatology Project
ISBA	Interactions between Soil, Biosphere, and Atmosphere

JRA-55	Japanese 55-year Reanalysis
PW	Precipitable water
SSMIS	Special Sensor Microwave Imager/Sounder
MERRA	Modern-Era Retrospective Analysis for Research and Applications
WMO	World Meteorological Organization
GLDAS	Global Land Data Assimilation System
GDAS	Global Data Assimilation System
CLM	Community Land Model
NLDAS	North American Land Data Assimilation System
NARR	North American Regional Reanalysis
PRISM	Parameter-Elevation Regressions on Independent Slopes Model
SNSR	Sierra Nevada Snow Reanalysis
CMC	Canadian Meteorological Centre
SNOTEL	Snowpack Telemetry
SNODAS	National Weather Service Snow Data Assimilation System
NWS	National Weather Service
GlobSnow	Global Snow Monitoring for Climate Research
ESA	European Space Agency

Symbols

M_p	Potential snowmelt
ρ	Density
L	Latent heat of fusion
R_s	Solar insolation
α	Albedo
$R_{l,in}$	Incoming longwave radiation
$R_{l,out}$	Outgoing longwave radiation
H	Sensible heat flux
LE	Latent heat flux
M_a	Actual snowmelt
SCA	Fractional snow cover area
SWE	Snow water equivalent
SWE_0	Initial SWE
SWE_n	SWE at time n
$M_{a,i}$	Actual snowmelt during time step i
T_B	Brightness temperature
ΔT_B	Brightness temperature difference between low and high frequency
A	Offset
B	Slope
$T_{B,18H}$	Horizontally polarized brightness temperatures at 18 GHz
$T_{B,37H}$	Horizontally polarized brightness temperatures at 37 GHz
f_c	Canopy fraction
F_t	Adjustment coefficient for canopy fraction
C_t	Adjustment coefficient for snow grain size
F_j	Percentage of grassland, deciduous forest, coniferous forest, and sparse forest
SD	Snow depth
f	Fraction of land cover
C	Empirical coefficient
T_g	Temperature of the soil–snow interface
T_a	Temperature of the atmosphere–snow interface
$SD(t)$	Snow depth varying with time
TG	Temperature gradient
$r(t)$	Snow grain size
r_0	Initial snow grain size
r_∞	Upper limit for snow grain size
t	Time
k	Empirical coefficient
l	Empirical coefficient

f_v	Snow volume fraction
$f_{v,0}$	Fresh snow volume fraction
$f_{v,\infty}$	Maximum f_v
b	Empirical coefficient of grain size
c	Empirical coefficient of snow volume
f_f	Forest fraction
SD_f	Forested component of snow depth
SD_0	Non-forested component of snow depth
A'	Snowpack radiation properties
B'	Snowpack attenuation properties
θ	Zenith angle
φ	Azimuth angle
z	Vertical location (snow depth)
θ'	Slant angle
φ'	Slant angle
$\mathfrak{k}_e$	Extinction coefficient
$\mathfrak{k}_a$	Absorption coefficient
T	Physical temperature of snow
$\mathfrak{k}_s^{bi}(\theta, \varphi, \theta', \varphi')$	Bistatic scattering coefficient
$\mathfrak{k}_s$	Scattering coefficient
θ_0	Observing zenith angle
$T_{up}(z')$	Upward brightness temperature
$T_{dn}(z')$	Downward brightness temperature
$\mathfrak{k}_s^{forward}$	Forward scattering coefficient
$\mathfrak{k}_s^{backward}$	Backward scattering coefficient
f'	Frequency
d_0	Snow diameter
P	Phase function
σ_{pq}^t	Total radar backscatter at polarization pq
σ_{pq}^s	Surface backscatter of the air–snow and snow–soil interfaces at polarization pq
σ_{pq}^v	Volume scattering of the snowpack at polarization pq
L'	Snowpack attenuation coefficient
T'	Power transmission coefficient at the air–snow interface
σ_{pq}^g	Scattering coefficient directly originating from soil
i	number of channels, indicates the (i.e., optical thickness and single scattering albedo), denotes the, is the and is the
σ_i^{obs}	Observed backscattering signal
σ_i^{est}	Estimated backscattering signal
x_i	Snow microstructure
$\overline{x}_i$	Mean of x_i
v	Error variance of radar measurements
vp	Variance of a priori constraint
τ_a	Absorption component of snow optical thickness
$\tau_a(f')$	Absorption part of optical thickness at frequency f'
V_s	Volume fraction of snow
k_0	SAR wave number
ε	Dielectric constant
$\acute{\varepsilon}$	Imaginary part of ε
φ_{flat}	Phase differences caused by changes in the distance between the target and satellite in flat terrain
φ_{topo}	Phase differences caused by changes in the distance between the target and satellite in complex terrain
φ_{atm}	Phase differences caused by variations of atmospheric propagation
φ_{noise}	Phase noise
φ_{snow}	Two-way propagation difference in snow relative to the air

k_i	Incoming radar beam vector
θ_i	Incidence angle
d_i	Thickness of layer i
r_i	Reflectivity of layer i
$T_{B, \, ground}$	Upward ground brightness temperature
$T_{B, \, air}$	Downward air brightness temperature
$r_{air\text{-}snow}$	Air–snow boundary reflectivity
$r_{ground\text{-}snow}$	Ground–snow boundary reflectivity

References

1. Clark, M.P.; Hendrikx, J.; Slater, A.G.; Kavetski, D.; Anderson, B.; Cullen, N.J.; Kerr, T.; Örn Hreinsson, E.; Woods, R.A. Representing spatial variability of snow water equivalent in hydrologic and land-surface models: A review. *Water Resour. Res.* **2011**, *47*, W07539. [CrossRef]
2. Sui, J.; Koehler, G. Rain-on-snow induced flood events in Southern Germany. *J. Hydrol.* **2001**, *252*, 205–220. [CrossRef]
3. Viviroli, D.; Archer, D.R.; Buytaert, W.; Fowler, H.J.; Greenwood, G.B.; Hamlet, A.F.; Huang, Y.; Koboltschnig, G.; Litaor, M.I.; López-Moreno, J.I.; et al. Climate change and mountain water resources: Overview and recommendations for research, management and policy. *Hydrol. Earth Syst. Sci.* **2011**, *15*, 471–504. [CrossRef]
4. Finger, D.; Heinrich, G.; Gobiet, A.; Bauder, A. Projections of future water resources and their uncertainty in a glacierized catchment in the Swiss Alps and the subsequent effects on hydropower production during the 21st century. *Water Resour. Res.* **2012**, *48*, W02521. [CrossRef]
5. Freudiger, D.; Kohn, I.; Stahl, K.; Weiler, M. Large-scale analysis of changing frequencies of rain-on-snow events with flood-generation potential. *Hydrol. Earth Syst. Sci.* **2014**, *18*, 2695–2709. [CrossRef]
6. Singh, P. *Snow and Glacier Hydrology*; Springer Science & Business Media: Berlin/Heidelberg, Germany, 2001; Volume 37.
7. Derksen, C.; Brown, R.; Mudryk, L.; Luojus, K. Terrestrial Snow Cover. In Arctic Report Card 2016. 2016. Available online: https://www.arctic.noaa.gov/Report-Card (accessed on 24 July 2022).
8. Nauslar, N.; Brown, T.J.; McEvoy, D.J.; Lareau, N. Record setting 2018 California wildfires [in "State of the Climate in 2018"]. *Bull. Am. Meteorol. Soc.* **2019**, *100*, S195–S196.
9. Mudryk, L.R.; Derksen, C.; Howell, S.; Laliberté, F.; Thackeray, C.; Sospedra-Alfonso, R.; Vionnet, V.; Kushner, P.J.; Brown, R. Canadian snow and sea ice: Historical trends and projections. *Cryosphere* **2018**, *12*, 1157–1176. [CrossRef]
10. Barnett, T.P.; Adam, J.C.; Lettenmaier, D.P. Potential impacts of a warming climate on water availability in snow-dominated regions. *Nature* **2005**, *438*, 303–309. [CrossRef]
11. Pirazzini, R.; Leppänen, L.; Picard, G.; Lopez-Moreno, J.I.; Marty, C.; Macelloni, G.; Kontu, A.; Von Lerber, A.; Tanis, C.M.; Schneebeli, M.; et al. European in-situ snow measurements: Practices and purposes. *Sensors* **2018**, *18*, 2016. [CrossRef]
12. Hatchett, B.J.; McEvoy, D.J. Exploring the origins of snow drought in the northern Sierra Nevada, California. *Earth Interact.* **2018**, *22*, 1–13. [CrossRef]
13. Wrzesien, M.L.; Durand, M.T.; Pavelsky, T.M.; Howat, I.M.; Margulis, S.A.; Huning, L.S. Comparison of methods to estimate snow water equivalent at the mountain range scale: A case study of the California Sierra Nevada. *J. Hydrometeorol.* **2017**, *18*, 1101–1119. [CrossRef]
14. Dozier, J.; Bair, E.H.; Davis, R.E. Estimating the spatial distribution of snow water equivalent in the world's mountains. *Wiley Interdiscip. Rev. Water* **2016**, *3*, 461–474. [CrossRef]
15. Shi, J.; Xiong, C.; Jiang, L. Review of snow water equivalent microwave remote sensing. *Sci. China Earth Sci.* **2016**, *59*, 731–745. [CrossRef]
16. Helmert, J.; Şensoy Şorman, A.; Alvarado Montero, R.; De Michele, C.; De Rosnay, P.; Dumont, M.; Finger, D.C.; Lange, M.; Picard, G.; Potopová, V.; et al. Review of snow data assimilation methods for hydrological, land surface, meteorological and climate models: Results from a cost harmosnow survey. *Geosciences* **2018**, *8*, 489. [CrossRef]
17. De Lannoy, G.J.; Reichle, R.H.; Arsenault, K.R.; Houser, P.R.; Kumar, S.; Verhoest, N.E.; Pauwels, V.R. Multiscale assimilation of Advanced Microwave Scanning Radiometer—EOS snow water equivalent and Moderate Resolution Imaging Spectroradiometer snow cover fraction observations in northern Colorado. *Water Resour. Res.* **2012**, *48*, W01522. [CrossRef]
18. Pulliainen, J.; Hallikainen, M. Retrieval of regional snow water equivalent from space-borne passive microwave observations. *Remote Sens. Environ.* **2001**, *75*, 76–85. [CrossRef]
19. Sorman, A.U.; Beser, O. Determination of snow water equivalent over the eastern part of Turkey using passive microwave data. *Hydrol. Process.* **2013**, *27*, 1945–1958. [CrossRef]
20. Liang, S.; Wang, J. *Advanced Remote Sensing: Terrestrial Information Extraction and Applications*; Academic Press: Cambridge, MA, USA, 2019.
21. Essery, R. Snowpack Modelling and Data Assimilation. ECMWF-WWRP/THORPEX Workshop on Polar Prediction. 2013. Available online: https://ecmwf.org/sites/default/files/elibrary/2013/13948-snowpack-modelling-and-data-assimilation.pdf (accessed on 24 July 2022).
22. Dong, C. Remote sensing, hydrological modeling and in situ observations in snow cover research: A review. *J. Hydrol.* **2018**, *561*, 573–583. [CrossRef]

23. Cline, D.W.; Bales, R.C.; Dozier, J. Estimating the spatial distribution of snow in mountain basins using remote sensing and energy balance modeling. *Water Resour. Res.* **1998**, *34*, 1275–1285. [CrossRef]

24. Guan, B.; Molotch, N.P.; Waliser, D.E.; Jepsen, S.M.; Painter, T.H.; Dozier, J. Snow water equivalent in the Sierra Nevada: Blending snow sensor observations with snowmelt model simulations. *Water Resour. Res.* **2013**, *49*, 5029–5046. [CrossRef]

25. Dozier, J. Spectral signature of alpine snow cover from the Landsat Thematic Mapper. *Remote Sens. Environ.* **1989**, *28*, 9–22. [CrossRef]

26. Nolin, A.W. Recent advances in remote sensing of seasonal snow. *J. Glaciol.* **2010**, *56*, 1141–1150. [CrossRef]

27. Grody, N.C.; Basist, A.N. Global identification of snowcover using SSM/I measurements. *IEEE Trans. Geosci. Remote Sens.* **1996**, *34*, 237–249. [CrossRef]

28. Foster, J.L.; Hall, D.K.; Kelly, R.E.J.; Chiu, L. Seasonal snow extent and snow mass in South America using SMMR and SSM/I passive microwave data (1979–2006). *Remote Sens. Environ.* **2009**, *113*, 291–305. [CrossRef]

29. Ulaby, F.T.; Long, D.G.; Blackwell, W.J.; Elachi, C.; Fung, A.K.; Ruf, C.; Sarabandi, K.; Zebker, H.A.; Van Zyl, J. *Microwave Radar and Radiometric Remote Sensing*; University of Michigan Press: Ann Arbor, MI, USA, 2014; Volume 4.

30. Chang, A.T.; Foster, J.L.; Hall, D.K. Nimbus-7 SMMR derived global snow cover parameters. *Ann. Glaciol.* **1987**, *9*, 39–44. [CrossRef]

31. Lemmetyinen, J.; Pulliainen, J.; Rees, A.; Kontu, A.; Qiu, Y.; Derksen, C. Multiple-layer adaptation of HUT snow emission model: Comparison with experimental data. *IEEE Trans. Geosci. Remote Sens.* **2010**, *48*, 2781–2794. [CrossRef]

32. Derksen, C. The contribution of AMSR-E 18.7 and 10.7 GHz measurements to improved boreal forest snow water equivalent retrievals. *Remote Sens. Environ.* **2008**, *112*, 2701–2710. [CrossRef]

33. Jiang, L.; Shi, J.; Tjuatja, S.; Chen, K.S.; Du, J.; Zhang, L. Estimation of snow water equivalence using the polarimetric scanning radiometer from the cold land processes experiments (CLPX03). *IEEE Geosci. Remote Sens. Lett.* **2010**, *8*, 359–363. [CrossRef]

34. Pan, J.; Durand, M.T.; Vander Jagt, B.J.; Liu, D. Application of a Markov Chain Monte Carlo algorithm for snow water equivalent retrieval from passive microwave measurements. *Remote Sens. Environ.* **2017**, *192*, 150–165. [CrossRef]

35. Picard, G.; Brucker, L.; Roy, A.; Dupont, F.; Fily, M.; Royer, A.; Harlow, C. Simulation of the microwave emission of multi-layered snowpacks using the Dense Media Radiative transfer theory: The DMRT-ML model. *Geosci. Model Dev.* **2013**, *6*, 1061–1078. [CrossRef]

36. Taheri, M.; Mohammadian, A.; Ganji, F.; Bigdeli, M.; Nasseri, M. Energy-based approaches in estimating actual evapotranspiration focusing on land surface temperature: A review of methods, concepts, and challenges. *Energies* **2022**, *15*, 1264. [CrossRef]

37. Slater, A.G.; Schlosser, C.A.; Desborough, C.E.; Pitman, A.J.; Henderson-Sellers, A.; Robock, A.; Vinnikov, K.Y.; Entin, J.; Mitchell, K.; Chen, F.; et al. The representation of snow in land surface schemes: Results from PILPS 2 (d). *J. Hydrometeorol.* **2001**, *2*, 7–25. [CrossRef]

38. Mortimer, C.; Mudryk, L.; Derksen, C.; Luojus, K.; Brown, R.; Kelly, R.; Tedesco, M. Evaluation of long-term Northern Hemisphere snow water equivalent products. *Cryosphere* **2020**, *14*, 1579–1594. [CrossRef]

39. Foster, J.L.; Sun, C.; Walker, J.P.; Kelly, R.; Chang, A.; Dong, J.; Powell, H. Quantifying the uncertainty in passive microwave snow water equivalent observations. *Remote Sens. Environ.* **2005**, *94*, 187–203. [CrossRef]

40. Durand, M.; Kim, E.J.; Margulis, S.A.; Molotch, N.P. A first-order characterization of errors from neglecting stratigraphy in forward and inverse passive microwave modeling of snow. *IEEE Geosci. Remote Sens. Lett.* **2011**, *8*, 730–734. [CrossRef]

41. Durand, M.; Liu, D. The need for prior information in characterizing snow water equivalent from microwave brightness temperatures. *Remote Sens. Environ.* **2012**, *126*, 248–257. [CrossRef]

42. Takala, M.; Luojus, K.; Pulliainen, J.; Derksen, C.; Lemmetyinen, J.; Kärnä, J.P.; Koskinen, J.; Bojkov, B. Estimating northern hemisphere snow water equivalent for climate research through assimilation of space-borne radiometer data and ground-based measurements. *Remote Sens. Environ.* **2011**, *115*, 3517–3529. [CrossRef]

43. Su, H.; Yang, Z.-L.; Dickinson, R.E.; Wilson, C.R.; Niu, G.-Y. Multisensor snow data assimilation at the continental scale: The value of Gravity Recovery and Climate Experiment terrestrial water storage information. *J. Geophys. Res. Atmos.* **2010**, *115*, D10104. [CrossRef]

44. WMO. *Guide to Meteorological Instruments and Methods of Observation*; WMO: Geneva, Switzerland, 1996.

45. Beaumont, R.M. Hood pressure pillow snow gage. *J. Appl. Meteorol. Climatol.* **1965**, *4*, 626–631. [CrossRef]

46. Cox, L.M.; Bartee, L.D.; Crook, A.G.; Farnes, P.E.; Smith, J.L. The care and feeding of snow pillows. In Proceedings of the 46th Annual Western Snow Conference, Otter Rock, OR, USA, 18–20 April 1978.

47. Johnson, J.B.; Marks, D. The detection and correction of snow water equivalent pressure sensor errors. *Hydrol. Process.* **2004**, *18*, 3513–3525. [CrossRef]

48. Engeset, R.; Sorteberg, H.; Udnaes, H. Snow pillows: Use and verification. In *Snow Engineering Recent Advances and Developments*; Routledge: London, UK, 2017; pp. 45–52.

49. Smith, C.D.; Kontu, A.; Laffin, R.; Pomeroy, J.W. An assessment of two automated snow water equivalent instruments during the WMO Solid Precipitation Intercomparison Experiment. *Cryosphere* **2017**, *11*, 101–116. [CrossRef]

50. Loijens, H. Measurement of snow water equivalent and soil moisture by natural gamma radiation. In Proceedings of the Canadian Hydrology Symposium, Winnipeg, MB, Canada, 11–14 August 1975; Department of the Environment: Ottawa, ON, Canada, 1975.

51. Young, G. A portable profiling snow gauge results of field tests on glaciers. In Proceedings of the 44th Western Snow Conference, Calgary, AB, Canada, 18–21 April 1976.

52. Li, X.; Zhang, L.; Weihermüller, L.; Jiang, L.; Vereecken, H. Measurement and simulation of topographic effects on passive microwave remote sensing over mountain areas: A case study from the Tibetan Plateau. *IEEE Trans. Geosci. Remote Sens.* **2013**, *52*, 1489–1501. [CrossRef]

53. Leppänen, L.; Kontu, A.; Vehviläinen, J.; Lemmetyinen, J.; Pulliainen, J. Comparison of traditional and optical grain-size field measurements with SNOWPACK simulations in a taiga snowpack. *J. Glaciol.* **2015**, *61*, 151–162. [CrossRef]

54. Kelly, R. The AMSR-E snow depth algorithm: Description and initial results. *J. Remote Sens. Soc. Jpn.* **2009**, *29*, 307–317.

55. Tedesco, M.; Narvekar, P.S. Assessment of the nasa amsr-e *SWE* product. *IEEE J. Sel. Top. Appl. Earth Obs. Remote Sens.* **2010**, *3*, 141–159. [CrossRef]

56. Goodison, B. Accuracy of snow samplers for measuring shallow snowpacks: An update. In Proceedings of the 35th Annual Meeting Eastern Snow Conference, Hanover, NH, USA, 2–3 February 1978.

57. Johnson, J.B.; Gelvin, A.B.; Duvoy, P.; Schaefer, G.L.; Poole, G.; Horton, G.D. Performance characteristics of a new electronic snow water equivalent sensor in different climates. *Hydrol. Process.* **2015**, *29*, 1418–1433. [CrossRef]

58. Sturm, M.; Taras, B.; Liston, G.E.; Derksen, C.; Jonas, T.; Lea, J. Estimating snow water equivalent using snow depth data and climate classes. *J. Hydrometeorol.* **2010**, *11*, 1380–1394. [CrossRef]

59. Dixon, D.; Boon, S. Comparison of the SnowHydro snow sampler with existing snow tube designs. *Hydrol. Process.* **2012**, *26*, 2555–2562. [CrossRef]

60. Largeron, C.; Dumont, M.; Morin, S.; Boone, A.; Lafaysse, M.; Metref, S.; Cosme, E.; Jonas, T.; Winstral, A.; Margulis, S.A. Toward snow cover estimation in mountainous areas using modern data assimilation methods: A review. *Front. Earth Sci.* **2020**, *8*, 325. [CrossRef]

61. Meromy, L.; Molotch, N.P.; Link, T.E.; Fassnacht, S.R.; Rice, R. Subgrid variability of snow water equivalent at operational snow stations in the western USA. *Hydrol. Process.* **2013**, *27*, 2383–2400. [CrossRef]

62. Schneider, D.; Molotch, N.P. Real-time estimation of snow water equivalent in the Upper Colorado River Basin using MODIS-based *SWE* Reconstructions and SNOTEL data. *Water Resour. Res.* **2016**, *52*, 7892–7910. [CrossRef]

63. Fassnacht, S.; Dressler, K.; Bales, R. Snow water equivalent interpolation for the Colorado River Basin from snow telemetry (SNOTEL) data. *Water Resour. Res.* **2003**, *39*, 1208. [CrossRef]

64. Zheng, Z.; Kirchner, P.; Bales, R. Topographic and vegetation effects on snow accumulation in the southern Sierra Nevada: A statistical summary from lidar data. *Cryosphere* **2016**, *10*, 257–269. [CrossRef]

65. Ni, K.S.; Nguyen, T.Q. An adaptable k-nearest neighbors algorithm for MMSE image interpolation. *IEEE Trans. Image Process.* **2009**, *18*, 1976–1987. [CrossRef] [PubMed]

66. Molotch, N.P.; Bales, R.C. Scaling snow observations from the point to the grid element: Implications for observation network design. *Water Resour. Res.* **2005**, *41*, W11421. [CrossRef]

67. Martinec, J.; Rango, A. Areal distribution of snow water equivalent evaluated by snow cover monitoring. *Water Resour. Res.* **1981**, *17*, 1480–1488. [CrossRef]

68. Molotch, N.; Guan, B.; Lestak, L. *Snow Water Equivalent (SWE) for Water Supply and Management in California. INSTAAR and NASA's Jet Propulsion Laboratory*; University of Colorado: Boulder, CO, USA, 2017; p. 64.

69. Molotch, N.P.; Margulis, S.A. Estimating the distribution of snow water equivalent using remotely sensed snow cover data and a spatially distributed snowmelt model: A multi-resolution, multi-sensor comparison. *Adv. Water Resour.* **2008**, *31*, 1503–1514. [CrossRef]

70. Molotch, N.P. Reconstructing snow water equivalent in the Rio Grande headwaters using remotely sensed snow cover data and a spatially distributed snowmelt model. *Hydrol. Process. Int. J.* **2009**, *23*, 1076–1089. [CrossRef]

71. Jepsen, S.M.; Molotch, N.P.; Williams, M.W.; Rittger, K.E.; Sickman, J.O. Interannual variability of snowmelt in the Sierra Nevada and Rocky Mountains, United States: Examples from two alpine watersheds. *Water Resour. Res.* **2012**, *48*, W02529. [CrossRef]

72. Girotto, M.; Margulis, S.A.; Durand, M. Probabilistic *SWE* reanalysis as a generalization of deterministic *SWE* reconstruction techniques. *Hydrol. Process.* **2014**, *28*, 3875–3895. [CrossRef]

73. Rittger, K.; Bair, E.H.; Kahl, A.; Dozier, J. Spatial estimates of snow water equivalent from reconstruction. *Adv. Water Resour.* **2016**, *94*, 345–363. [CrossRef]

74. Zheng, Z.; Molotch, N.P.; Oroza, C.A.; Conklin, M.H.; Bales, R.C. Spatial snow water equivalent estimation for mountainous areas using wireless-sensor networks and remote-sensing products. *Remote Sens. Environ.* **2018**, *215*, 44–56. [CrossRef]

75. Bair, E.H.; Rittger, K.; Davis, R.E.; Painter, T.H.; Dozier, J. Validating reconstruction of snow water equivalent in California's Sierra Nevada using measurements from the NASA Airborne Snow Observatory. *Water Resour. Res.* **2016**, *52*, 8437–8460. [CrossRef]

76. Dozier, J.; Painter, T.H.; Rittger, K.; Frew, J.E. Time–space continuity of daily maps of fractional snow cover and albedo from MODIS. *Adv. Water Resour.* **2008**, *31*, 1515–1526. [CrossRef]

77. Kongoli, C.; Dean, C.A.; Helfrich, S.R.; Ferraro, R.R. The retrievals of snow cover extent and snow water equivalent from a blended passive microwave–interactive multi-sensor snow product. In Proceedings of the 63rd Eastern Snow Conference, Newark, DE, USA, 7–9 June 2006.

78. Ulaby, F.T.; Stiles, W.H. The active and passive microwave response to snow parameters: 2. Water equivalent of dry snow. *J. Geophys. Res. Oceans* **1980**, *85*, 1045–1049. [CrossRef]

79. Luojus, K.; Pulliainen, J.; Takala, M.; Lemmetyinen, J.; Mortimer, C.; Derksen, C.; Mudryk, L.; Moisander, M.; Hiltunen, M.; Smolander, T.; et al. GlobSnow v3. 0 Northern Hemisphere snow water equivalent dataset. *Sci. Data* **2021**, *8*, 163. [CrossRef]

80. Vander Jagt, B.J.; Durand, M.T.; Margulis, S.A.; Kim, E.J.; Molotch, N.P. The effect of spatial variability on the sensitivity of passive microwave measurements to snow water equivalent. *Remote Sens. Environ.* **2013**, *136*, 163–179. [CrossRef]
81. Foster, J.; Chang, A.; Hall, D. Comparison of snow mass estimates from a prototype passive microwave snow algorithm, a revised algorithm and a snow depth climatology. *Remote Sens. Environ.* **1997**, *62*, 132–142. [CrossRef]
82. Kelly, R.E.; Chang, A.T.; Tsang, L.; Foster, J.L. A prototype AMSR-E global snow area and snow depth algorithm. *IEEE Trans. Geosci. Remote Sens.* **2003**, *41*, 230–242. [CrossRef]
83. Clifford, D. Global estimates of snow water equivalent from passive microwave instruments: History, challenges and future developments. *Int. J. Remote Sens.* **2010**, *31*, 3707–3726. [CrossRef]
84. Gu, L.; Ren, R.; Zhao, K.; Li, X. Snow depth and snow cover retrieval from FengYun3B microwave radiation imagery based on a snow passive microwave unmixing method in Northeast China. *J. Appl. Remote Sens.* **2014**, *8*, 084682. [CrossRef]
85. Gu, L.; Ren, R.; Li, X. Snow depth retrieval based on a multifrequency dual-polarized passive microwave unmixing method from mixed forest observations. *IEEE Trans. Geosci. Remote Sens.* **2016**, *54*, 7279–7291. [CrossRef]
86. Gu, L.; Ren, R.; Li, X.; Zhao, K. Snow Depth retrieval based on a multifrequency passive microwave unmixing method for saline-alkaline land in the western Jilin province of China. *IEEE J. Sel. Top. Appl. Earth Obs. Remote Sens.* **2018**, *11*, 2210–2222. [CrossRef]
87. Liu, X.; Jiang, L.; Wang, G.; Hao, S.; Chen, Z. Using a linear unmixing method to improve passive microwave snow depth retrievals. *IEEE J. Sel. Top. Appl. Earth Obs. Remote Sens.* **2018**, *11*, 4414–4429. [CrossRef]
88. Long, D.G.; Daum, D.L. Spatial resolution enhancement of SSM/I data. *IEEE Trans. Geosci. Remote Sens.* **1998**, *36*, 407–417. [CrossRef]
89. Long, D.G.; Brodzik, M.J. Optimum image formation for spaceborne microwave radiometer products. *IEEE Trans. Geosci. Remote Sens.* **2015**, *54*, 2763–2779. [CrossRef]
90. Liu, J.; Melloh, R.A.; Woodcock, C.E.; Davis, R.E.; Ochs, E.S. The effect of viewing geometry and topography on viewable gap fractions through forest canopies. *Hydrol. Process.* **2004**, *18*, 3595–3607. [CrossRef]
91. Vuyovich, C.M.; Jacobs, J.M.; Daly, S.F. Comparison of passive microwave and modeled estimates of total watershed *SWE* in the continental United States. *Water Resour. Res.* **2014**, *50*, 9088–9102. [CrossRef]
92. Lemmetyinen, J.; Derksen, C.; Pulliainen, J.; Strapp, W.; Toose, P.; Walker, A.; Tauriainen, S.; Pihlflyckt, J.; Karna, J.P.; Hallikainen, M.T. A comparison of airborne microwave brightness temperatures and snowpack properties across the boreal forests of Finland and Western Canada. *IEEE Trans. Geosci. Remote Sens.* **2009**, *47*, 965–978. [CrossRef]
93. Lemmetyinen, J.; Kontu, A.; Rautiainen, K.; Vehvilainen, J.; Pulliainen, J. Technical Assistance for the Deployment of an X-to Ku-Band Scatterometer during the Nosrex II Experiment; Final Report, ESA ESTEC Contract, 2011(22671/09). 2011. Available online: https://earth.esa.int/eogateway/documents/20142/37627/NoSREx-I-II-III_Final_Reports.pdf (accessed on 24 July 2022).
94. Derksen, C.; Walker, A.; Goodison, B. Evaluation of passive microwave snow water equivalent retrievals across the boreal forest/tundra transition of western Canada. *Remote Sens. Environ.* **2005**, *96*, 315–327. [CrossRef]
95. Foster, J.L.; Hall, D.K.; Chang, A.T.; Rango, A.; Wergin, W.; Erbe, E. Effects of snow crystal shape on the scattering of passive microwave radiation. *IEEE Trans. Geosci. Remote Sens.* **1999**, *37*, 1165–1168. [CrossRef]
96. Wiesmann, A.; Mätzler, C. Microwave emission model of layered snowpacks. *Remote Sens. Environ.* **1999**, *70*, 307–316. [CrossRef]
97. Mätzler, C. Applications of the interaction of microwaves with the natural snow cover. *Remote Sens. Rev.* **1987**, *2*, 259–387. [CrossRef]
98. Hallikainen, M.; Ulaby, F.; Abdelrazik, M. Dielectric properties of snow in the 3 to 37 GHz range. *IEEE Trans. Antennas Propag.* **1986**, *34*, 1329–1340. [CrossRef]
99. Derksen, C.; MacKay, M. The Canadian boreal snow water equivalent band. *Atmos.-Ocean* **2006**, *44*, 305–320. [CrossRef]
100. Brown, R.D.; Brasnett, B.; Robinson, D. Gridded North American monthly snow depth and snow water equivalent for GCM evaluation. *Atmos.-Ocean* **2003**, *41*, 1–14. [CrossRef]
101. Pan, J.; Durand, M.; Sandells, M.; Lemmetyinen, J.; Kim, E.J.; Pulliainen, J.; Kontu, A.; Derksen, C. Differences between the HUT snow emission model and MEMLS and their effects on brightness temperature simulation. *IEEE Trans. Geosci. Remote Sens.* **2015**, *54*, 2001–2019. [CrossRef]
102. Chang, A.T.C.; Foster, J.L.; Hall, D.K.; Rango, A.; Hartline, B.K. Snow water equivalent estimation by microwave radiometry. *Cold Reg. Sci. Technol.* **1982**, *5*, 259–267. [CrossRef]
103. Hallikainen, M. Retrieval of snow water equivalent from Nimbus-7 SMMR data: Effect of land-cover categories and weather conditions. *IEEE J. Ocean. Eng.* **1984**, *9*, 372–376. [CrossRef]
104. Cao, M.S.; Li, P.J.; Robinson, D.A.; Spies, T.E.; Kukla, G. Evaluation and primary application of microwave remote sensing SMMR derived snow cover in Western China. *Remote Sens. Environ. China* **1993**, *8*, 260–269.
105. Che, T.; Li, X.; Jin, R.; Armstrong, R.; Zhang, T. Snow depth derived from passive microwave remote-sensing data in China. *Ann. Glaciol.* **2008**, *49*, 145–154. [CrossRef]
106. Sun, Z.-W.; Shi, J.-C.; Jiang, L.-M.; Yang, H.; Zhang, L.-X. Development of snow depth and snow water equivalent algorithm in Western China using passive microwave remote sensing data. *Adv. Earth Sci.* **2006**, *21*, 1363–1369.
107. Chang, S.; Shi, J.; Jiang, L.; Zhang, L.; Yang, H. Improved snow depth retrieval algorithm in China area using passive microwave remote sensing data. In Proceedings of the 2009 IEEE International Geoscience and Remote Sensing Symposium, Cape Town, South Africa, 12–17 July 2009; IEEE: Piscataway, NJ, USA, 2009.

108. Jiang, L.; Wang, P.; Zhang, L.; Yang, H.; Yang, J. Improvement of snow depth retrieval for FY3B-MWRI in China. *Sci. China Earth Sci.* **2014**, *57*, 1278–1292. [CrossRef]

109. Josberger, E.G.; Mognard, N.M. A passive microwave snow depth algorithm with a proxy for snow metamorphism. *Hydrol. Process.* **2002**, *16*, 1557–1568. [CrossRef]

110. Grippa, M.; Mognard, N.; Le Toan, T.; Josberger, E.G. Siberia snow depth climatology derived from SSM/I data using a combined dynamic and static algorithm. *Remote Sens. Environ.* **2004**, *93*, 30–41. [CrossRef]

111. Biancamaria, S.; Mognard, N.M.; Boone, A.; Grippa, M.; Josberger, E.G. A satellite snow depth multi-year average derived from SSM/I for the high latitude regions. *Remote Sens. Environ.* **2008**, *112*, 2557–2568. [CrossRef]

112. Jiang, L.; Shi, J.; Tjuatja, S.; Dozier, J.; Chen, K.; Zhang, L. A parameterized multiple-scattering model for microwave emission from dry snow. *Remote Sens. Environ.* **2007**, *111*, 357–366. [CrossRef]

113. Pulliainen, J.T.; Grandell, J.; Hallikainen, M.T. HUT snow emission model and its applicability to snow water equivalent retrieval. *IEEE Trans. Geosci. Remote Sens.* **1999**, *37*, 1378–1390. [CrossRef]

114. Tsang, L.; Chen, C.-T.; Chang, A.T.C.; Guo, J.; Ding, K.H. Dense media radiative transfer theory based on quasicrystalline approximation with applications to passive microwave remote sensing of snow. *Radio Sci.* **2000**, *35*, 731–749. [CrossRef]

115. Wang, H.; Pulliainen, J.; Hallikainen, M. Application of strong fluctuation theory to microwave emission from dry snow. *Prog. Electromagn. Res.* **2000**, *29*, 39–55. [CrossRef]

116. Ding, K.-H.; Xu, X.; Tsang, L. Electromagnetic scattering by bicontinuous random microstructures with discrete permittivities. *IEEE Trans. Geosci. Remote Sens.* **2010**, *48*, 3139–3151. [CrossRef]

117. Chang, W.; Tan, S.; Lemmetyinen, J.; Tsang, L.; Xu, X.; Yueh, S.H. Dense media radiative transfer applied to SnowScat and SnowSAR. *IEEE J. Sel. Top. Appl. Earth Obs. Remote Sens.* **2014**, *7*, 3811–3825. [CrossRef]

118. Tsang, L.; Ding, K.; Wen, B. Dense media radiative transfer theory for dense discrete random media with particles of multiple sizes and permittivities. *Prog. Electromagn. Res.* **1992**, *6*, 181–225. [CrossRef]

119. Chen, C.-T.; Tsang, L.; Guo, J.; Chang, A.T.C.; Ding, K.-H. Frequency dependence of scattering and extinction of dense media based on three-dimensional simulations of Maxwell's equations with applications to snow. *IEEE Trans. Geosci. Remote Sens.* **2003**, *41*, 1844–1852. [CrossRef]

120. Boyarskii, D.; Etkin, V. Two flow model of wet snow microwave emissivity. In Proceedings of the IGARSS'94-1994 IEEE International Geoscience and Remote Sensing Symposium, Pasadena, CA, USA, 8–12 August 1994; IEEE: Piscataway, NJ, USA, 1994.

121. Royer, A.; Roy, A.; Montpetit, B.; Saint-Jean-Rondeau, O.; Picard, G.; Brucker, L.; Langlois, A. Comparison of commonly-used microwave radiative transfer models for snow remote sensing. *Remote Sens. Environ.* **2017**, *190*, 247–259. [CrossRef] [PubMed]

122. Tsang, L.; Kong, J.A.; Shin, R.T. Theory of Microwave Remote Sensing. 1985. Available online: https://ntrs.nasa.gov/citations/19850058641 (accessed on 24 July 2022).

123. Fung, A.K. *Microwave Scattering and Emission Models and Their Applications*; Artech House: Norwood, MA, USA, 1994.

124. Mätzler, C. Improved Born approximation for scattering of radiation in a granular medium. *J. Appl. Phys.* **1998**, *83*, 6111–6117. [CrossRef]

125. Van de Hulst, H. *Light Scattering by Small Particles, $9.21*; Courier Corporation: New York, NY, USA; Dover, DE, USA, 1957.

126. Hallikainen, M.T.; Ulaby, F.T.; Van Deventer, T.E. Extinction behavior of dry snow in the 18-to 90-GHz range. *IEEE Trans. Geosci. Remote Sens.* **1987**, *6*, 737–745. [CrossRef]

127. Roy, V.; Goïta, K.; Royer, A.; Walker, A.E.; Goodison, B.E. Snow water equivalent retrieval in a Canadian boreal environment from microwave measurements using the HUT snow emission model. *IEEE Trans. Geosci. Remote Sens.* **2004**, *42*, 1850–1859. [CrossRef]

128. Ulaby, F.T.; Moore, R.K.; Fung, A.K. *Microwave Remote Sensing: Active and Passive: Volume 3: From Theory to Applications*; Artech House: London, UK, 1986.

129. Chuah, H.; Tan, H. A Monte Carlo method for radar backscatter from a half-space random medium. *IEEE Trans. Geosci. Remote Sens.* **1989**, *27*, 86–93. [CrossRef]

130. Flanner, M.G.; Arnheim, J.B.; Cook, J.M.; Dang, C.; He, C.; Huang, X.; Singh, D.; Skiles, S.M.; Whicker, C.A.; Zender, C.S. SNICAR-ADv3: A community tool for modeling spectral snow albedo. *Geosci. Model Dev.* **2021**, *14*, 7673–7704. [CrossRef]

131. Lapuerta, M.; González-Correa, S.; Ballesteros, R.; Cereceda-Balic, F.; Moosmüller, H. Albedo reduction for snow surfaces contaminated with soot aerosols: Comparison of experimental results and models. *Aerosol Sci. Technol.* **2022**, *56*, 847–858. [CrossRef]

132. Jin, Y.-Q. *Electromagnetic Scattering Modelling for Quantitative Remote Sensing*; World Scientific: Singapore, 1993.

133. Matzler, C.; Wegmuller, U. Dielectric properties of freshwater ice at microwave frequencies. *J. Phys. D Appl. Phys.* **1987**, *20*, 1623. [CrossRef]

134. Mätzler, C. *Thermal Microwave Radiation: Applications for Remote Sensing*; IET: Stevenage, UK, 2006; Volume 52.

135. Borghese, F.; Denti, P.; Saija, R. *Scattering from Model Nonspherical Particles: Theory and Applications to Environmental Physics*; Springer Science & Business Media: Berlin/Heidelberg, Germany, 2007.

136. Chopra, K.; Reddy, G. Optically selective coatings. *Pramana* **1986**, *27*, 193–217. [CrossRef]

137. Ishiniaru, A.; Kuga, Y. Attenuation constant of a coherent field in a dense distribution of particles. *JOSA* **1982**, *72*, 1317–1320. [CrossRef]

138. Kong, J.A.; Tsang, L.; Ding, K.-H.; Ao, C.O. *Scattering of Electromagnetic Waves: Numerical Simulations*; John Wiley & Sons: Hoboken, NJ, USA, 2004.

139. Tsang, L.; Pan, J.; Liang, D.; Li, Z.; Cline, D.W.; Tan, Y. Modeling active microwave remote sensing of snow using dense media radiative transfer (DMRT) theory with multiple-scattering effects. *IEEE Trans. Geosci. Remote Sens.* **2007**, *45*, 990–1004. [CrossRef]

140. Du, J.; Shi, J.; Rott, H. Comparison between a multi-scattering and multi-layer snow scattering model and its parameterized snow backscattering model. *Remote Sens. Environ.* **2010**, *114*, 1089–1098. [CrossRef]

141. Stogryn, A. A study of the microwave brightness temperature of snow from the point of view of strong fluctuation theory. *IEEE Trans. Geosci. Remote Sens.* **1986**, *2*, 220–231. [CrossRef]

142. Etchevers, P.; Martin, E.; Brown, R.; Fierz, C.; Lejeune, Y.; Bazile, E.; Boone, A.; Dai, Y.J.; Essery, R.; Fernandez, A.; et al. Validation of the energy budget of an alpine snowpack simulated by several snow models (Snow MIP project). *Ann. Glaciol.* **2004**, *38*, 150–158. [CrossRef]

143. Butt, M.; Kelly, R. Estimation of snow depth in the UK using the HUT snow emission model. *Int. J. Remote Sens.* **2008**, *29*, 4249–4267. [CrossRef]

144. Butt, M.J. A comparative study of Chang and HUT models for UK snow depth retrieval. *Int. J. Remote Sens.* **2009**, *30*, 6361–6379. [CrossRef]

145. Pulliainen, J. Mapping of snow water equivalent and snow depth in boreal and sub-arctic zones by assimilating space-borne microwave radiometer data and ground-based observations. *Remote Sens. Environ.* **2006**, *101*, 257–269. [CrossRef]

146. Dai, L.; Che, T.; Wang, J.; Zhang, P. Snow depth and snow water equivalent estimation from AMSR-E data based on a priori snow characteristics in Xinjiang, China. *Remote Sens. Environ.* **2012**, *127*, 14–29. [CrossRef]

147. Che, T.; Dai, L.; Zheng, X.; Li, X.; Zhao, K. Estimation of snow depth from passive microwave brightness temperature data in forest regions of northeast China. *Remote Sens. Environ.* **2016**, *183*, 334–349. [CrossRef]

148. Forman, B.A.; Reichle, R.H. Using a support vector machine and a land surface model to estimate large-scale passive microwave brightness temperatures over snow-covered land in North America. *IEEE J. Sel. Top. Appl. Earth Obs. Remote Sens.* **2014**, *8*, 4431–4441. [CrossRef]

149. Xiao, X.; Zhang, T.; Zhong, X.; Shao, W.; Li, X. Support vector regression snow-depth retrieval algorithm using passive microwave remote sensing data. *Remote Sens. Environ.* **2018**, *210*, 48–64. [CrossRef]

150. Bair, E.H.; Abreu Calfa, A.; Rittger, K.; Dozier, J. Using machine learning for real-time estimates of snow water equivalent in the watersheds of Afghanistan. *Cryosphere* **2018**, *12*, 1579–1594. [CrossRef]

151. Breiman, L. Random forests. *Mach. Learn.* **2001**, *45*, 5–32. [CrossRef]

152. Andreadis, K.M.; Lettenmaier, D.P. Assimilating remotely sensed snow observations into a macroscale hydrology model. *Adv. Water Resour.* **2006**, *29*, 872–886. [CrossRef]

153. Clark, M.P.; Slater, A.G.; Barrett, A.P.; Hay, L.E.; McCabe, G.J.; Rajagopalan, B.; Leavesley, G.H. Assimilation of snow covered area information into hydrologic and land-surface models. *Adv. Water Resour.* **2006**, *29*, 1209–1221. [CrossRef]

154. Nagler, T.; Rott, H.; Malcher, P.; Müller, F. Assimilation of meteorological and remote sensing data for snowmelt runoff forecasting. *Remote Sens. Environ.* **2008**, *112*, 1408–1420. [CrossRef]

155. Leisenring, M.; Moradkhani, H. Snow water equivalent prediction using Bayesian data assimilation methods. *Stoch. Environ. Res. Risk Assess.* **2011**, *25*, 253–270. [CrossRef]

156. Liu, Y.; Peters-Lidard, C.D.; Kumar, S.; Foster, J.L.; Shaw, M.; Tian, Y.; Fall, G.M. Assimilating satellite-based snow depth and snow cover products for improving snow predictions in Alaska. *Adv. Water Resour.* **2013**, *54*, 208–227. [CrossRef]

157. Blöschl, G. Scaling issues in snow hydrology. *Hydrol. Process.* **1999**, *13*, 2149–2175. [CrossRef]

158. Brown, R.D.; Fang, B.; Mudryk, L. Update of Canadian historical snow survey data and analysis of snow water equivalent trends, 1967–2016. *Atmos.-Ocean* **2019**, *57*, 149–156. [CrossRef]

159. Robertson, F.R.; Bosilovich, M.G.; Chen, J.; Miller, T.L. The effect of satellite observing system changes on MERRA water and energy fluxes. *J. Clim.* **2011**, *24*, 5197–5217. [CrossRef]

160. Liston, G.E.; Pielke, R.A., Sr.; Greene, E.M. Improving first-order snow-related deficiencies in a regional climate model. *J. Geophys. Res. Atmos.* **1999**, *104*, 19559–19567. [CrossRef]

161. Rodell, M.; Houser, P.R.; Jambor, U.E.A.; Gottschalck, J.; Mitchell, K.; Meng, C.J. The global land data assimilation system. *Bull. Am. Meteorol. Soc.* **2004**, *85*, 381–394. [CrossRef]

162. Malik, N.; Bookhagen, B.; Marwan, N.; Kurths, J. Analysis of spatial and temporal extreme monsoonal rainfall over South Asia using complex networks. *Clim. Dyn.* **2012**, *39*, 971–987. [CrossRef]

163. Cressman, G.P. An operational objective analysis system. *Mon. Weather Rev.* **1959**, *87*, 367–374. [CrossRef]

164. Drusch, M.; Vasiljevic, D.; Viterbo, P. ECMWF's global snow analysis: Assessment and revision based on satellite observations. *J. Appl. Meteorol.* **2004**, *43*, 1282–1294. [CrossRef]

165. Dee, D.P.; Uppala, S.M.; Simmons, A.J.; Berrisford, P.; Poli, P.; Kobayashi, S.; Andrae, U.; Balmaseda, M.A.; Balsamo, G.; Bauer, D.P.; et al. The ERA-Interim reanalysis: Configuration and performance of the data assimilation system. *Q. J. R. Meteorol. Soc.* **2011**, *137*, 553–597. [CrossRef]

166. Gandin, L. The general problem of the optimum interpolation and extrapolation of meteorological fields (Optimum interpolation and extrapolation of meteorological fields). *Tr. Gl. Geofiz. Observ.* **1965**, *168*, 75–83.

167. Liston, G.E.; Hiemstra, C.A. A simple data assimilation system for complex snow distributions (SnowAssim). *J. Hydrometeorol.* **2008**, *9*, 989–1004. [CrossRef]

168. Brasnett, B. A global analysis of snow depth for numerical weather prediction. *J. Appl. Meteorol.* **1999**, *38*, 726–740. [CrossRef]

169. de Rosnay, P.; Balsamo, G.; Albergel, C.; Muñoz-Sabater, J.; Isaksen, L. Initialisation of land surface variables for numerical weather prediction. *Surv. Geophys.* **2014**, *35*, 607–621. [CrossRef]

170. De Rosnay, P.; Isaksen, L.; Dahoui, M. Snow data assimilation at ECMWF. *ECMWF Newsl.* **2015**, *143*, 26–31.

171. Piazzi, G.; Thirel, G.; Campo, L.; Gabellani, S. A particle filter scheme for multivariate data assimilation into a point-scale snowpack model in an Alpine environment. *Cryosphere* **2018**, *12*, 2287–2306. [CrossRef]

172. Talagrand, O. Assimilation of observations, an introduction (gtspecial issueltdata assimilation in meteology and oceanography: Theory and practice). *J. Meteorol. Soc. Jpn. Ser. II* **1997**, *75*, 191–209. [CrossRef]

173. Winstral, A.; Magnusson, J.; Schirmer, M.; Jonas, T. The bias-detecting ensemble: A new and efficient technique for dynamically incorporating observations into physics-based, multilayer snow models. *Water Resour. Res.* **2019**, *55*, 613–631. [CrossRef]

174. Gelb, A. *Applied Optimal Estimation*; MIT Press: Cambridge, MA, USA, 1974.

175. Jazwinski, A. *Stochastic Processes and Filtering Theory*; Academic Press: Cambridge, MA, USA, 1970; Volume 64.

176. Miller, R.N.; Ghil, M.; Gauthiez, F. Advanced data assimilation in strongly nonlinear dynamical systems. *J. Atmos. Sci.* **1994**, *51*, 1037–1056. [CrossRef]

177. Dong, J.; Walker, J.P.; Houser, P.R.; Sun, C. Scanning multichannel microwave radiometer snow water equivalent assimilation. *J. Geophys. Res. Atmos.* **2007**, *112*, D07108. [CrossRef]

178. Evensen, G. Sequential data assimilation with a nonlinear quasi-geostrophic model using Monte Carlo methods to forecast error statistics. *J. Geophys. Res. Oceans* **1994**, *99*, 10143–10162. [CrossRef]

179. Burgers, G.; Van Leeuwen, P.J.; Evensen, G. Analysis scheme in the ensemble Kalman filter. *Mon. Weather Rev.* **1998**, *126*, 1719–1724. [CrossRef]

180. Evensen, G.; Van Leeuwen, P.J. An ensemble Kalman smoother for nonlinear dynamics. *Mon. Weather Rev.* **2000**, *128*, 1852–1867. [CrossRef]

181. Kumar, S.V.; Reichle, R.H.; Peters-Lidard, C.D.; Koster, R.D.; Zhan, X.; Crow, W.T.; Eylander, J.B.; Houser, P.R. A land surface data assimilation framework using the land information system: Description and applications. *Adv. Water Resour.* **2008**, *31*, 1419–1432. [CrossRef]

182. Charrois, L.; Cosme, E.; Dumont, M.; Lafaysse, M.; Morin, S.; Libois, Q.; Picard, G. On the assimilation of optical reflectances and snow depth observations into a detailed snowpack model. *Cryosphere* **2016**, *10*, 1021–1038. [CrossRef]

183. Larue, F.; Royer, A.; De Sève, D.; Roy, A.; Picard, G.; Vionnet, V.; Cosme, E. Simulation and assimilation of passive microwave data using a snowpack model coupled to a calibrated radiative transfer model over northeastern Canada. *Water Resour. Res.* **2018**, *54*, 4823–4848. [CrossRef]

184. DeChant, C.M.; Moradkhani, H. Improving the characterization of initial condition for ensemble streamflow prediction using data assimilation. *Hydrol. Earth Syst. Sci.* **2011**, *15*, 3399–3410. [CrossRef]

185. Margulis, S.A.; Cortés, G.; Girotto, M.; Durand, M. A Landsat-era Sierra Nevada snow reanalysis (1985–2015). *J. Hydrometeorol.* **2016**, *17*, 1203–1221. [CrossRef]

186. Cortés, G.; Margulis, S. Impacts of El Niño and La Niña on interannual snow accumulation in the Andes: Results from a high-resolution 31 year reanalysis. *Geophys. Res. Lett.* **2017**, *44*, 6859–6867. [CrossRef]

187. Margulis, S.A.; Girotto, M.; Cortés, G.; Durand, M. A particle batch smoother approach to snow water equivalent estimation. *J. Hydrometeorol.* **2015**, *16*, 1752–1772. [CrossRef]

188. Li, D.; Durand, M.; Margulis, S.A. Estimating snow water equivalent in a Sierra Nevada watershed via spaceborne radiance data assimilation. *Water Resour. Res.* **2017**, *53*, 647–671. [CrossRef]

189. Carroll, T.R. A procedure to incorporate snow course data into the National Weather Service River Forecast System. In Proceedings of the Workshop on Modelling of Snow Cover Runoff, Hanover, NH, USA, 26–28 September 1978; CRREL: Hanover, NH, USA, 1978.

190. Day, G.N. *A Methodology for Updating a Conceptual Snow Model with Snow Measurements*; The Johns Hopkins University: Baltimore, MD, USA, 1990.

191. Smyth, E.J.; Raleigh, M.S.; Small, E.E. Particle filter data assimilation of monthly snow depth observations improves estimation of snow density and *SWE*. *Water Resour. Res.* **2019**, *55*, 1296–1311. [CrossRef]

192. Magnusson, J.; Gustafsson, D.; Hüsler, F.; Jonas, T. Assimilation of point *SWE* data into a distributed snow cover model comparing two contrasting methods. *Water Resour. Res.* **2014**, *50*, 7816–7835. [CrossRef]

193. Hedrick, A.R.; Marks, D.; Havens, S.; Robertson, M.; Johnson, M.; Sandusky, M.; Marshall, H.P.; Kormos, P.R.; Bormann, K.J.; Painter, T.H. Direct insertion of NASA Airborne Snow Observatory-derived snow depth time series into the iSnobal energy balance snow model. *Water Resour. Res.* **2018**, *54*, 8045–8063. [CrossRef]

194. Margulis, S.A.; Fang, Y.; Li, D.; Lettenmaier, D.P.; Andreadis, K. The utility of infrequent snow depth images for deriving continuous space-time estimates of seasonal snow water equivalent. *Geophys. Res. Lett.* **2019**, *46*, 5331–5340. [CrossRef]

195. Kim, R.S.; Durand, M.; Li, D.; Baldo, E.; Margulis, S.A.; Dumont, M.; Morin, S. Estimating alpine snow depth by combining multifrequency passive radiance observations with ensemble snowpack modeling. *Remote Sens. Environ.* **2019**, *226*, 1–15. [CrossRef]

196. Saloranta, T.M. Operational snow mapping with simplified data assimilation using the seNorge snow model. *J. Hydrol.* **2016**, *538*, 314–325. [CrossRef]

197. Aalstad, K.; Westermann, S.; Schuler, T.V.; Boike, J.; Bertino, L. Ensemble-based assimilation of fractional snow-covered area satellite retrievals to estimate the snow distribution at Arctic sites. *Cryosphere* **2018**, *12*, 247–270. [CrossRef]

198. Painter, T.H.; Berisford, D.F.; Boardman, J.W.; Bormann, K.J.; Deems, J.S.; Gehrke, F.; Hedrick, A.; Joyce, M.; Laidlaw, R.; Marks, D.; et al. The Airborne Snow Observatory: Fusion of scanning lidar, imaging spectrometer, and physically-based modeling for mapping snow water equivalent and snow albedo. *Remote Sens. Environ.* **2016**, *184*, 139–152. [CrossRef]

199. Durand, M.; Margulis, S.A. Feasibility test of multifrequency radiometric data assimilation to estimate snow water equivalent. *J. Hydrometeorol.* **2006**, *7*, 443–457. [CrossRef]

200. Carrassi, A.; Bocquet, M.; Bertino, L.; Evensen, G. Data assimilation in the geosciences: An overview of methods, issues, and perspectives. *Wiley Interdiscip. Rev. Clim. Chang.* **2018**, *9*, e535. [CrossRef]

201. Shi, J.; Dozier, J. Estimation of snow water equivalence using SIR-C/X-SAR: I. Inferring snow density and subsurface properties. *IEEE Trans. Geosci. Remote Sens.* **2000**, *38*, 2465–2474.

202. Shi, J.; Dozier, J. Estimation of snow water equivalence using SIR-C/X-SAR, part II: Inferring snow depth and particle size. *IEEE Trans. Geosci. Remote Sens.* **2000**, *38*, 2475–2488.

203. Drinkwater, M.R.; Long, D.G.; Bingham, A.W. Greenland snow accumulation estimates from satellite radar scatterometer data. *J. Geophys. Res. Atmos.* **2001**, *106*, 33935–33950. [CrossRef]

204. Rott, H.; Yueh, S.H.; Cline, D.W.; Duguay, C.; Essery, R.; Haas, C.; Heliere, F.; Kern, M.; Macelloni, G.; Malnes, E.; et al. Cold regions hydrology high-resolution observatory for snow and cold land processes. *Proc. IEEE* **2010**, *98*, 752–765. [CrossRef]

205. Cui, Y.; Xiong, C.; Lemmetyinen, J.; Shi, J.; Jiang, L.; Peng, B.; Li, H.; Zhao, T.; Ji, D.; Hu, T. Estimating snow water equivalent with backscattering at X and Ku band based on absorption loss. *Remote Sens.* **2016**, *8*, 505. [CrossRef]

206. Xiong, C.; Shi, J. The potential for estimating snow depth with QuikScat data and a snow physical model. *IEEE Geosci. Remote Sens. Lett.* **2017**, *14*, 1156–1160. [CrossRef]

207. Lemmetyinen, J.; Derksen, C.; Rott, H.; Macelloni, G.; King, J.; Schneebeli, M.; Wiesmann, A.; Leppänen, L.; Kontu, A.; Pulliainen, J. Retrieval of effective correlation length and snow water equivalent from radar and passive microwave measurements. *Remote Sens.* **2018**, *10*, 170. [CrossRef]

208. Zhu, J.; Tan, S.; King, J.; Derksen, C.; Lemmetyinen, J.; Tsang, L. Forward and inverse radar modeling of terrestrial snow using SnowSAR data. *IEEE Trans. Geosci. Remote Sens.* **2018**, *56*, 7122–7132. [CrossRef]

209. King, J.; Derksen, C.; Toose, P.; Langlois, A.; Larsen, C.; Lemmetyinen, J.; Marsh, P.; Montpetit, B.; Roy, A.; Rutter, N.; et al. The influence of snow microstructure on dual-frequency radar measurements in a tundra environment. *Remote Sens. Environ.* **2018**, *215*, 242–254. [CrossRef]

210. Shi, J.; Yueh, S.; Cline, D. On estimation of snow water equivalence using L-band and Ku-band radar in IGARSS 2003. In Proceedings of the 2003 IEEE International Geoscience and Remote Sensing Symposium, Toulouse, France, 21–25 July 2003; IEEE: Piscataway, NJ, USA, 2003.

211. Yueh, S.H.; Dinardo, S.J.; Akgiray, A.; West, R.; Cline, D.W.; Elder, K. Airborne Ku-band polarimetric radar remote sensing of terrestrial snow cover. *IEEE Trans. Geosci. Remote Sens.* **2009**, *47*, 3347–3364. [CrossRef]

212. Brogioni, M.; Macelloni, G.; Paloscia, S.; Pampaloni, P.; Pettinato, S.; Santi, E.; X'iong, C.; Crepaz, A. Sensitivity analysis of microwave backscattering and emission to snow water equivalent: Synergy of dual sensor observations. In Proceedings of the 2011 XXXth URSI General Assembly and Scientific Symposium, Istanbul, Turkey, 13–20 August 2011; IEEE: Piscataway, NJ, USA, 2011.

213. Shi, J.; Dong, X.; Zhao, T.; Liu, H.; Wang, Z.; Du, J.; Jiang, L.; Du, Y.; Ji, D.; Xiong, C. Observing Earth's water cycle from space. In Proceedings of the SPIE international Asia-Pacific Environmental Remote Sensing Symposium, Beijing, China, 13 October 2014.

214. Lundberg, A.; Thunehed, H.; Bergström, J. Impulse radar snow surveys—Influence of snow density. *Hydrol. Res.* **2000**, *31*, 1–14. [CrossRef]

215. McGrath, D.; Webb, R.; Shean, D.; Bonnell, R.; Marshall, H.P.; Painter, T.H.; Molotch, N.P.; Elder, K.; Hiemstra, C.; Brucker, L. Spatially extensive ground-penetrating radar snow depth observations during NASA's 2017 SnowEx campaign: Comparison with In situ, airborne, and satellite observations. *Water Resour. Res.* **2019**, *55*, 10026–10036. [CrossRef]

216. Meehan, T.G.; Marshall, H.P.; Bradford, J.H.; Hawley, R.L.; Overly, T.B.; Lewis, G.; Graeter, K.; Osterberg, E.; McCarthy, F. Reconstruction of historical surface mass balance, 1984–2017 from GreenTrACS multi-offset ground-penetrating radar. *J. Glaciol.* **2021**, *67*, 219–228. [CrossRef]

217. Panzer, B.; Gomez-Garcia, D.; Leuschen, C.; Paden, J.; Rodriguez-Morales, F.; Patel, A.; Markus, T.; Holt, B.; Gogineni, P. An ultra-wideband, microwave radar for measuring snow thickness on sea ice and mapping near-surface internal layers in polar firn. *J. Glaciol.* **2013**, *59*, 244–254. [CrossRef]

218. Arnold, E.; Leuschen, C.; Rodriguez-Morales, F.; Li, J.; Paden, J.; Hale, R.; Keshmiri, S. CReSIS airborne radars and platforms for ice and snow sounding. *Ann. Glaciol.* **2020**, *61*, 58–67. [CrossRef]

219. Yan, J.-B.; Gogineni, S.; Rodriguez-Morales, F.; Gomez-Garcia, D.; Paden, J.; Li, J.; Leuschen, C.J.; Braaten, D.A.; Richter-Menge, J.A.; Farrell, S.L.; et al. Airborne Measurements of Snow Thickness: Using ultrawide-band frequency-modulated-continuous-wave radars. *IEEE Geosci. Remote Sens. Mag.* **2017**, *5*, 57–76. [CrossRef]

220. Rekioua, B.; Davy, M.; Ferro-Famil, L.; Tebaldini, S. Snowpack permittivity profile retrieval from tomographic SAR data. *Comptes Rendus Phys.* **2017**, *18*, 57–65. [CrossRef]

221. Deeb, E.J.; Forster, R.R.; Kane, D.L. Monitoring snowpack evolution using interferometric synthetic aperture radar on the North Slope of Alaska, USA. *Int. J. Remote Sens.* **2011**, *32*, 3985–4003. [CrossRef]

222. Lei, Y.; Siqueira, P.; Treuhaft, R. A dense medium electromagnetic scattering model for the InSAR correlation of snow. *Radio Sci.* **2016**, *51*, 461–480. [CrossRef]

223. Guneriussen, T.; Hogda, K.A.; Johnsen, H.; Lauknes, I. InSAR for estimation of changes in snow water equivalent of dry snow. *IEEE Trans. Geosci. Remote Sens.* **2001**, *39*, 2101–2108. [CrossRef]

224. Moller, D.; Andreadis, K.M.; Bormann, K.J.; Hensley, S.; Painter, T.H. Mapping snow depth from ka-band interferometry: Proof of concept and comparison with scanning lidar retrievals. *IEEE Geosci. Remote Sens. Lett.* **2017**, *14*, 886–890. [CrossRef]

225. Rees, A.; Lemmetyinen, J.; Derksen, C.; Pulliainen, J.; English, M. Observed and modelled effects of ice lens formation on passive microwave brightness temperatures over snow covered tundra. *Remote Sens. Environ.* **2010**, *114*, 116–126. [CrossRef]

226. Tedesco, M.; Jeyaratnam, J. *AMSR-E/AMSR2 Unified L3 Global Daily 25 Km EASE-Grid Snow Water Equivalent, Version 1*; NASA National Snow and Ice Data Center Distributed Active Archive Center: Boulder, CO, USA, 2019.

227. Chang, A.T.C.; Foster, J.L.; Hall, D. Satellite sensor estimates of northern hemisphere snow volume. *Int. J. Remote Sens.* **1990**, *11*, 167–171. [CrossRef]

228. Brown, R.D.; Braaten, R.O. Spatial and temporal variability of Canadian monthly snow depths, 1946–1995. *Atmos.-Ocean* **1998**, *36*, 37–54. [CrossRef]

229. Krenke, A. *Edited by National Snow and Ice Data Center, Former Soviet Union Hydrological Snow Surveys, 1966–1996, Version 1*; NSIDC: National Snow and Ice Data Center: Boulder, CO, USA, 2004.

230. Sturm, M.; Holmgren, J.; Liston, G.E. A seasonal snow cover classification system for local to global applications. *J. Clim.* **1995**, *8*, 1261–1283. [CrossRef]

231. Knowles, K.; Njoku, E.G.; Armstrong, R.; Brodzik, M.J. *Nimbus-7 SMMR Pathfinder Daily EASE-Grid Brightness Temperatures, Version 1, from 1979 to 1987*; NASA DAAC, National Snow and Ice Data Center: Boulder, CO, USA, 2000.

232. Hollinger, J.P.; Peirce, J.L.; Poe, G.A. SSM/I instrument evaluation. *IEEE Trans. Geosci. Remote Sens.* **1990**, *28*, 781–790. [CrossRef]

233. Saha, S.; Nadiga, S.; Thiaw, C.; Wang, J.; Wang, W.; Zhang, Q.; Van den Dool, H.M.; Pan, H.L.; Moorthi, S.; Behringer, D.; et al. The NCEP climate forecast system. *J. Clim.* **2006**, *19*, 3483–3517. [CrossRef]

234. Xie, P.; Chen, M.; Shi, W. CPC unified gauge-based analysis of global daily precipitation. In Proceedings of the 24th Conference on Hydrology, Atlanta, GA, USA, 18–22 January 2010.

235. Xie, P.; Arkin, P.A. Global precipitation: A 17-year monthly analysis based on gauge observations, satellite estimates, and numerical model outputs. *Bull. Am. Meteorol. Soc.* **1997**, *78*, 2539–2558. [CrossRef]

236. Ek, M.B.; Mitchell, K.E.; Lin, Y.; Rogers, E.; Grunmann, P.; Koren, V.; Gayno, G.; Tarpley, J.D. Implementation of Noah land surface model advances in the National Centers for Environmental Prediction operational mesoscale Eta model. *J. Geophys. Res. Atmos.* **2003**, *108*, 8851. [CrossRef]

237. Kopp, T. The air force global weather central cloud analysis model. In Proceedings of the 15th Conference on Weather Analysis and Forecasting, Norfolk, VA, USA, 19–23 August 1996.

238. Helfrich, S.R.; McNamara, D.; Ramsay, B.H.; Baldwin, T.; Kasheta, T. Enhancements to, and forthcoming developments in the Interactive Multisensor Snow and Ice Mapping System (IMS). *Hydrol. Process. Int. J.* **2007**, *21*, 1576–1586. [CrossRef]

239. Foster, J.L.; Hall, D.K.; Eylander, J.B.; Riggs, G.A.; Nghiem, S.V.; Tedesco, M.; Kim, E.; Montesano, P.M.; Kelly, R.E.; Casey, K.A.; et al. A blended global snow product using visible, passive microwave and scatterometer satellite data. *Int. J. Remote Sens.* **2011**, *32*, 1371–1395. [CrossRef]

240. Uppala, S.M.; Kållberg, P.W.; Simmons, A.J.; Andrae, U.; Bechtold, V.D.C.; Fiorino, M.; Gibson, J.K.; Haseler, J.; Hernandez, A.; Kelly, G.A.; et al. The ERA-40 re-analysis. *Q. J. R. Meteorol. Soc. A J. Atmos. Sci. Appl. Meteorol. Phys. Oceanogr.* **2005**, *131*, 2961–3012. [CrossRef]

241. Reichler, T.; Kim, J. Uncertainties in the climate mean state of global observations, reanalyses, and the GFDL climate model. *J. Geophys. Res. Atmos.* **2008**, *113*, D05106. [CrossRef]

242. Douville, H.; Royer, J.F.; Mahfouf, J.F. A new snow parameterization for the Meteo-France climate model. *Clim. Dyn.* **1995**, *12*, 21–35. [CrossRef]

243. Bian, Q.; Xu, Z.; Zhao, L.; Zhang, Y.-F.; Zheng, H.; Shi, C.; Zhang, S.; Xie, C.; Yang, Z.-L. Evaluation and intercomparison of multiple snow water equivalent products over the Tibetan Plateau. *J. Hydrometeorol.* **2019**, *20*, 2043–2055. [CrossRef]

244. Dutra, E.; Balsamo, G.; Viterbo, P.; Miranda, P.M.; Beljaars, A.; Schär, C.; Elder, K. An improved snow scheme for the ECMWF land surface model: Description and offline validation. *J. Hydrometeorol.* **2010**, *11*, 899–916. [CrossRef]

245. Kapnick, S.B.; Delworth, T.L. Controls of global snow under a changed climate. *J. Clim.* **2013**, *26*, 5537–5562. [CrossRef]

246. Balsamo, G.; Albergel, C.; Beljaars, A.; Boussetta, S.; Cloke, H.; Dee, D.; Dutra, E.; Muñoz-Sabater, J.; Pappenberger, F.; De Rosnay, P.; et al. ERA-Interim/Land: A global land water resources dataset. *Hydrol. Earth Syst. Sci. Discuss.* **2013**, *10*, 14705–14745.

247. Adler, R.F.; Huffman, G.J.; Chang, A.; Ferraro, R.; Xie, P.P.; Janowiak, J.; Rudolf, B.; Schneider, U.; Curtis, S.; Bolvin, D.; et al. The version-2 global precipitation climatology project (GPCP) monthly precipitation analysis (1979–present). *J. Hydrometeorol.* **2003**, *4*, 1147–1167. [CrossRef]

248. Muñoz Sabater, J. *ERA5-Land Hourly Data from 1981 to Present*; Copernicus Climate Change Service (C3S) Climate Data Store (CDS): Reading, UK, 2019; Volume 10.

249. Brun, E.; Vionnet, V.; Boone, A.; Decharme, B.; Peings, Y.; Valette, R.; Karbou, F.; Morin, S. Simulation of northern Eurasian local snow depth, mass, and density using a detailed snowpack model and meteorological reanalyses. *J. Hydrometeorol.* **2013**, *14*, 203–219. [CrossRef]

250. Kobayashi, S.; Ota, Y.; Harada, Y.; Ebita, A.; Moriya, M.; Onoda, H.; Onogi, K.; Kamahori, H.; Kobayashi, C.; Endo, H.; et al. The JRA-55 reanalysis: General specifications and basic characteristics. *J. Meteorol. Soc. Jpn. Ser. II* **2015**, *93*, 5–48. [CrossRef]

251. Sellers, P.J.; Mintz, Y.C.S.Y.; Sud, Y.E.A.; Dalcher, A. A simple biosphere model (SiB) for use within general circulation models. *J. Atmos. Sci.* **1986**, *43*, 505–531. [CrossRef]

252. Onogi, K.; Koide, H.; Sakamoto, M.; Kobayashi, S.; Tsutsui, J.; Hatsushika, H.; Matsumoto, T.; Yamazaki, N.; Kamahori, H.; Takahashi, K.; et al. JRA-25: Japanese 25-year re-analysis project—Progress and status. *Q. J. R. Meteorol. Soc. A J. Atmos. Sci. Appl. Meteorol. Phys. Oceanogr.* **2005**, *131*, 3259–3268. [CrossRef]

253. Rienecker, M.M.; Suarez, M.J.; Gelaro, R.; Todling, R.; Bacmeister, J.; Liu, E.; Bosilovich, M.G.; Schubert, S.D.; Takacs, L.; Kim, G.K.; et al. MERRA: NASA's modern-era retrospective analysis for research and applications. *J. Clim.* **2011**, *24*, 3624–3648. [CrossRef]

254. Reichle, R.H.; Liu, Q.; Koster, R.D.; Draper, C.S.; Mahanama, S.P.; Partyka, G.S. Land surface precipitation in MERRA-2. *J. Clim.* **2017**, *30*, 1643–1664. [CrossRef]

255. Koster, R.D.; Suarez, M.J.; Ducharne, A.; Stieglitz, M.; Kumar, P. A catchment-based approach to modeling land surface processes in a general circulation model: 1. Model structure. *J. Geophys. Res. Atmos.* **2000**, *105*, 24809–24822. [CrossRef]

256. Stieglitz, M.; Ducharne, A.; Koster, R.; Suarez, M. The impact of detailed snow physics on the simulation of snow cover and subsurface thermodynamics at continental scales. *J. Hydrometeorol.* **2001**, *2*, 228–242. [CrossRef]

257. Liang, X.; Lettenmaier, D.P.; Wood, E.F.; Burges, S.J. A simple hydrologically based model of land surface water and energy fluxes for general circulation models. *J. Geophys. Res. Atmos.* **1994**, *99*, 14415–14428. [CrossRef]

258. Koster, R.D.; Suarez, M.J. The components of a 'SVAT'scheme and their effects on a GCM's hydrological cycle. *Adv. Water Resour.* **1994**, *17*, 61–78. [CrossRef]

259. Bonan, G.B.; Oleson, K.W.; Vertenstein, M.; Levis, S.; Zeng, X.; Dai, Y.; Dickinson, R.E.; Yang, Z.-L. The land surface climatology of the Community Land Model coupled to the NCAR Community Climate Model. *J. Clim.* **2002**, *15*, 3123–3149. [CrossRef]

260. Mitchell, K.E.; Lohmann, D.; Houser, P.R.; Wood, E.F.; Schaake, J.C.; Robock, A.; Cosgrove, B.A.; Sheffield, J.; Duan, Q.; Luo, L.; et al. The multi-institution North American Land Data Assimilation System (NLDAS): Utilizing multiple GCIP products and partners in a continental distributed hydrological modeling system. *J. Geophys. Res. Atmos.* **2004**, *109*, D07S90. [CrossRef]

261. Xia, Y.; Mitchell, K.; Ek, M.; Sheffield, J.; Cosgrove, B.; Wood, E.; Luo, L.; Alonge, C.; Wei, H.; Meng, J.; et al. Continental-scale water and energy flux analysis and validation for the North American Land Data Assimilation System project phase 2 (NLDAS-2): 1. Intercomparison and application of model products. *J. Geophys. Res. Atmos.* **2012**, *117*, D03109. [CrossRef]

262. Xia, Y.; Mitchell, K.; Ek, M.; Cosgrove, B.; Sheffield, J.; Luo, L.; Alonge, C.; Wei, H.; Meng, J.; Livneh, B.; et al. Continental-scale water and energy flux analysis and validation for North American Land Data Assimilation System project phase 2 (NLDAS-2): 2. Validation of model-simulated streamflow. *J. Geophys. Res. Atmos.* **2012**, *117*, D03110. [CrossRef]

263. Mesinger, F.; DiMego, G.; Kalnay, E.; Mitchell, K.; Shafran, P.C.; Ebisuzaki, W.; Jović, D.; Woollen, J.; Rogers, E.; Berbery, E.H.; et al. North American regional reanalysis. *Bull. Am. Meteorol. Soc.* **2006**, *87*, 343–360. [CrossRef]

264. Daly, C.; Neilson, R.P.; Phillips, D.L. A statistical-topographic model for mapping climatological precipitation over mountainous terrain. *J. Appl. Meteorol. Climatol.* **1994**, *33*, 140–158. [CrossRef]

265. Salzmann, N.; Mearns, L.O. Assessing the performance of multiple regional climate model simulations for seasonal mountain snow in the Upper Colorado River Basin. *J. Hydrometeorol.* **2012**, *13*, 539–556. [CrossRef]

266. Carroll, T.; Cline, D.; Fall, G.; Nilsson, A.; Li, L.; Rost, A. NOHRSC operations and the simulation of snow cover properties for the coterminous US. In Proceedings of the 69th Annual Meeting of the Western Snow Conference, Sun Valley, ID, USA, 17–19 April 2001.

267. Clow, D.W.; Nanus, L.; Verdin, K.L.; Schmidt, J. Evaluation of SNODAS snow depth and snow water equivalent estimates for the Colorado Rocky Mountains, USA. *Hydrol. Process.* **2012**, *26*, 2583–2591. [CrossRef]

268. Hedrick, A.; Marshall, H.P.; Winstral, A.; Elder, K.; Yueh, S.; Cline, D. Independent evaluation of the SNODAS snow depth product using regional-scale lidar-derived measurements. *Cryosphere* **2015**, *9*, 13–23. [CrossRef]

269. Kunkee, D.B.; Poe, G.A.; Boucher, D.J.; Swadley, S.D.; Hong, Y.; Wessel, J.E.; Uliana, E.A. Design and evaluation of the first special sensor microwave imager/sounder. *IEEE Trans. Geosci. Remote Sens.* **2008**, *46*, 863–883. [CrossRef]

270. Kunkee, D.B.; Poe, G.A.; Boucher, D.J.; Swadley, S.D.; Hong, Y.; Wessel, J.E.; Uliana, E.A. Passive microwave measurements of snow-covered forest areas in EMAC'95. *IEEE Trans. Geosci. Remote Sens.* **1999**, *37*, 2699–2705.

271. Kontu, A.; Lemmetyinen, J.; Pulliainen, J.; Seppänen, J.; Hallikainen, M.T. Observation and modeling of the microwave brightness temperature of snow-covered frozen lakes and wetlands. *IEEE Trans. Geosci. Remote Sens.* **2013**, *52*, 3275–3288. [CrossRef]

272. Lemmetyinen, J.; Derksen, C.; Toose, P.; Proksch, M.; Pulliainen, J.; Kontu, A.; Rautiainen, K.; Seppänen, J.; Hallikainen, M. Simulating seasonally and spatially varying snow cover brightness temperature using HUT snow emission model and retrieval of a microwave effective grain size. *Remote Sens. Environ.* **2015**, *156*, 71–95. [CrossRef]

273. Tedesco, M.; Kim, E.J. Intercomparison of electromagnetic models for passive microwave remote sensing of snow. *IEEE Trans. Geosci. Remote Sens.* **2006**, *44*, 2654–2666. [CrossRef]

274. Brown, R.; Brasnett, B. The Canadian Meteorological Centre global daily snow depth analysis, 1998–2011: Overview, experience and applications. In Proceedings of the 68th Eastern Snow Conference, Montreal, QC, Canada, 14–16 June 2011.

275. Hersbach, H.; Bell, B.; Berrisford, P.; Hirahara, S.; Horányi, A.; Muñoz-Sabater, J.; Nicolas, J.; Peubey, C.; Radu, R.; Schepers, D.; et al. The ERA5 global reanalysis. *Q. J. R. Meteorol. Soc.* **2020**, *146*, 1999–2049. [CrossRef]